



**NAVAL
POSTGRADUATE
SCHOOL**

MONTEREY, CALIFORNIA

THESIS

**TWO DIMENSIONAL ACOUSTIC PROPAGATION
THROUGH OCEANIC INTERNAL SOLITARY WAVES:
WEAK SCATTERING THEORY AND NUMERICAL
SIMULATION**

by

Aaron C. Young

June 2006

Thesis Advisor:
Second Reader:

John Colosi
D. Benjamin Reeder

Approved for public release; distribution is unlimited.

THIS PAGE INTENTIONALLY LEFT BLANK

REPORT DOCUMENTATION PAGE			Form Approved OMB No. 0704-0188	
Public reporting burden for this collection of information is estimated to average 1 hour per response, including the time for reviewing instruction, searching existing data sources, gathering and maintaining the data needed, and completing and reviewing the collection of information. Send comments regarding this burden estimate or any other aspect of this collection of information, including suggestions for reducing this burden, to Washington headquarters Services, Directorate for Information Operations and Reports, 1215 Jefferson Davis Highway, Suite 1204, Arlington, VA 22202-4302, and to the Office of Management and Budget, Paperwork Reduction Project (0704-0188) Washington DC 20503.				
1. AGENCY USE ONLY (Leave blank)		2. REPORT DATE June 2006	3. REPORT TYPE AND DATES COVERED Master's Thesis	
4. TITLE AND SUBTITLE: Two Dimensional Acoustic Propagation Through Oceanic Internal Solitary Waves: Weak Scattering Theory and Numerical Simulation			5. FUNDING NUMBERS	
6. AUTHOR(S) Young, Aaron C.				
7. PERFORMING ORGANIZATION NAME(S) AND ADDRESS(ES) Naval Postgraduate School Monterey, CA 93943-5000			8. PERFORMING ORGANIZATION REPORT NUMBER	
9. SPONSORING /MONITORING AGENCY NAME(S) AND ADDRESS(ES) N/A			10. SPONSORING/MONITORING AGENCY REPORT NUMBER	
11. SUPPLEMENTARY NOTES The views expressed in this thesis are those of the author and do not reflect the official policy or position of the Department of Defense or the U.S. Government.				
12a. DISTRIBUTION / AVAILABILITY STATEMENT Approved for public release; distribution is unlimited			12b. DISTRIBUTION CODE	
13. ABSTRACT Internal solitary waves, or solitons, are often generated in coastal or continental shelf regions when tidal currents advect stratified water over bathymetric relief, creating an internal tide which non-linearly evolves into one or more solitons. A major consequence of solitons in a stratified environment is the vertical displacement of water parcels which can lead to sound speed variability of order 10m/s with spatial scales of order 100 meters and timescales of order minutes. Thus significant variations in sonar performance on both surface based ships and submarines can be expected. An understanding into the nature of acoustic propagation through these waves is vital for future development of sonar prediction systems. This research investigates acoustic normal mode propagation through solitons using a 2D parabolic equation simulation and weak acoustic scattering theory whose primary physics is a single scatter Bragg mechanism. To simplify the theory, a Gaussian soliton model is developed that compares favorably to the results from a traditional sech^2 soliton model. The theory of sound through a Gaussian soliton was then tested against the numerical simulation under conditions of various acoustic frequency, source depths, soliton position relative to the source and soliton number. The theoretical results compare favorably with numerical simulations at 75, 150 and 300-Hz. Higher frequencies need to be tested to determine the limits of the first order theory. Higher order theory will then be needed to address even higher frequencies and to deal with weakly excited modes. This research is the first step in moving from a state of observing acoustic propagation through solitons, to one of predicting it.				
14. SUBJECT TERMS Oceanography, Weak Scattering Theory, Bragg Scattering, Soliton, Mode Coupling, Mode Energy, Acoustic Propagation, 2D Parabolic Equation, Internal Solitary Wave			15. NUMBER OF PAGES 83	
			16. PRICE CODE	
17. SECURITY CLASSIFICATION OF REPORT Unclassified	18. SECURITY CLASSIFICATION OF THIS PAGE Unclassified	19. SECURITY CLASSIFICATION OF ABSTRACT Unclassified	20. LIMITATION OF ABSTRACT UL	

THIS PAGE INTENTIONALLY LEFT BLANK

Approved for public release; distribution is unlimited.

**TWO DIMENSIONAL ACOUSTIC PROPAGATION THROUGH OCEANIC
INTERNAL SOLITARY WAVES: WEAK SCATTERING THEORY AND
NUMERICAL SIMULATION**

Aaron C. Young
Lieutenant Commander, Royal Australian Navy
B.Sc., University of New South Wales, 1995
Graduate Diploma of Meteorology, Bureau Meteorology, 2000

Submitted in partial fulfillment of the
requirements for the degree of

MASTER OF SCIENCE IN PHYSICAL OCEANOGRAPHY

from the

**NAVAL POSTGRADUATE SCHOOL
June 2006**

Author: Aaron C. Young

Approved by: John Colosi
Thesis Advisor

D. Benjamin Reeder
Second Reader

Mary Batteen
Chairman, Department of Oceanography

THIS PAGE INTENTIONALLY LEFT BLANK

ABSTRACT

Internal solitary waves, or solitons, are often generated in coastal or continental shelf regions when tidal currents advect stratified water over bathymetric relief, creating an internal tide which non-linearly evolves into one or more solitons. A major consequence of solitons in a stratified environment is the vertical displacement of water parcels which can lead to sound speed variability of order 10m/s with spatial scales of order 100 meters and timescales of order minutes. Thus significant variations in sonar performance on both surface based ships and submarines can be expected. An understanding into the nature of acoustic propagation through these waves is vital for future development of sonar prediction systems. This research investigates acoustic normal mode propagation through solitons using a 2D parabolic equation simulation and weak acoustic scattering theory whose primary physics is a single scatter Bragg mechanism. To simplify the theory, a Gaussian soliton model is developed that compares favorably to the results from a traditional sech^2 soliton model. The theory of sound through a Gaussian soliton was then tested against the numerical simulation under conditions of various acoustic frequency, source depths, soliton position relative to the source and soliton number. The theoretical results compare favorably with numerical simulations at 75, 150 and 300-Hz. Higher frequencies need to be tested to determine the limits of the first order theory. Higher order theory will then be needed to address even higher frequencies and to deal with weakly excited modes. This research is the first step in moving from a state of observing acoustic propagation through solitons, to one of predicting it.

THIS PAGE INTENTIONALLY LEFT BLANK

TABLE OF CONTENTS

I.	INTRODUCTION.....	1
A.	BACKGROUND	1
	1. Shallow Water Acoustics and the Importance of Internal Solitary Waves.....	1
	2. Statement of Research	3
II.	METHODS OF ANALYSIS	5
A.	PARABOLIC EQUATION METHOD.....	5
	1. The Parabolic Equation.....	5
	2. Boundary Conditions.....	6
	3. Starting Field.....	7
	4. Background Environment.....	8
	5. Solutions to the Parabolic Equation Using the Split Step Fourier Algorithm.....	10
B.	SOLITARY WAVE MODELING	10
	1. Single Soliton	10
	2. Soliton Wave Packet	16
C.	THE PARABOLIC EQUATION IN MODE FORM	17
	1. Perturbation Theory	18
	2. Sound Through Solitons	19
	3. The Gaussian Soliton	20
III.	RESULTS	25
A.	SECH² VERSUS GAUSSIAN SOLITON.....	25
	1. Single Wave	25
	2. Wave Packet	31
B.	VARIATION OF SINGLE SOLITON POSITION.....	34
	1. Numerical Results	34
	2. Theoretical Results.....	38
C.	VARIATION OF POSITION WITH A SOLITON WAVE PACKET.....	48
	1. Numerical Results	48
	2. Theoretical Results.....	49
D.	VARIATIONS IN SOURCE DEPTH	53
	1. Single Soliton	53
	2. Wave Packet	56
IV.	CONCLUSION	59
	LIST OF REFERENCES	63
	INITIAL DISTRIBUTION LIST	65

THIS PAGE INTENTIONALLY LEFT BLANK

LIST OF FIGURES

Figure 1.	The background sound speed profile used in this study. The water column is divided into three layers and a hyperbolic tangent function is used to transition between the layers and the thermocline; and between the water column and the bottom.....9	9
Figure 2.	Simulation of the total acoustic pressure field in decibels for a 75-Hz source at 60m.11	11
Figure 3.	To test mode energy conservation, the model is run with just the background sound speed environment, a frequency of 75-Hz and a source depth of 60m. The first plot shows the mode variance for each mode with only the first 7 modes being trapped. The mode energies $ A_n ^2(r)$ are represented in the second plot.....12	12
Figure 4.	To test mode energy conservation, the model is run with just the background sound speed environment, a frequency of 150-Hz and a source depth of 60m. The first plot shows the mode variance for each mode with only the first 12 modes being trapped. The mode energies $ A_n ^2(r)$ are represented in the second plot.....13	13
Figure 5.	To test mode energy conservation, the model is run with just the background sound speed environment, a frequency of 300-Hz and a source depth of 60m. The first plot shows the mode variance for each mode with only the first 20 modes being trapped. The mode energies $ A_n ^2(r)$ are represented in the second plot.....14	14
Figure 6.	A hyperbolic tangent function is used to transition the soliton amplitude to the background environment.....15	15
Figure 7.	Total sound speed field with a sech^2 shaped soliton at a range of 2.5km. The soliton width is 100m and the maximum amplitude is 10m.16	16
Figure 8.	Total sound speed field with a sech^2 shaped soliton wave packet. The solitons are at ranges of 2.5, 3 and 3.5km and have constant width of 100m. The maximum amplitudes are 10, 5 and 2.5m respectively.17	17
Figure 9.	A comparison of the sech^2 and Gaussian wave forms.23	23
Figure 10.	Mode energy $ A_n ^2(r)$ comparison between a sech^2 (red) and a Gaussian (blue) soliton shape for a single wave with a source depth of 60m and a frequency of 150-Hz. Similar results appear for all three frequencies. By visual inspection there is very little difference between the two shapes.26	26
Figure 11.	Relative mode energy $10\log_{10}\left(\frac{ A_n ^2}{ A_{n0} ^2}\right)$ between trapped modes for a single soliton, for all three frequencies at a range of 5km. The soliton is located at 2.5km. These results were obtained from averaging the mode energy of the last 1000m and comparing the difference between the two shapes in logarithmic form. The values which are not close to zero (e.g.	

	mode 9 at 150-Hz and mode 18 at 300-Hz) are discussed in Figures 12 to 14.....	27
Figure 12.	Mode energy $ A_n ^2(r)$ of a single soliton for both soliton forms, comparing the highest outlying mode to the adjacent mode energy at 75-Hz with a source depth of 60m. Mode 2 showed the greatest energy difference in decibels. Clearly mode 1 energy values are virtually indistinguishable between both shapes. The obvious difference between mode 2 values shows the sensitivity of shape to the phase at low energy modes. These modes, however can be ignored as their mode energy contributes almost nothing to the entire acoustic pressure field.	28
Figure 13.	Mode energy $ A_n ^2(r)$ of a single soliton for both soliton forms, comparing the highest outlying mode to the adjacent mode energy at 150-Hz with a source depth of 60m. Mode 9 showed the greatest energy difference in decibels. Clearly mode 8 energy values are virtually indistinguishable between both shapes. The obvious difference between mode 9 values shows the sensitivity of shape to the phase at low energy modes. These modes, however can be ignored as their mode energy contributes almost nothing to the entire acoustic pressure field.	29
Figure 14.	Mode energy $ A_n ^2(r)$ of a single soliton for both soliton forms, comparing the highest outlying mode to the adjacent mode energy at 300-Hz with a source depth of 60m. Mode 18 showed the greatest energy difference in decibels. Clearly mode 17 energy values are virtually indistinguishable between both shapes. The obvious difference between mode 18 values shows the sensitivity of shape to the phase at low energy modes. These modes, however can be ignored as their mode energy contributes almost nothing to the entire acoustic pressure field.	30
Figure 15.	Parametric plot of mode energy for the sech^2 and Gaussian solitons; for 75, 150 and 300-Hz. The clear linear relationship demonstrates the validity of using a Gaussian shaped soliton in place of the sech^2 form.	31
Figure 16.	Relative mode energy $10\log_{10}\left(\frac{ A_n ^2}{ A_{n0} ^2}\right)$ between trapped modes for a soliton packet, for all three frequencies, at a range of 5km. The soliton packet is located at 2.5km. These results were obtained from averaging the mode energy of the last 1000m and comparing the difference between the two shapes in logarithmic form.	32
Figure 17.	Mode energy $ A_n ^2(r)$ for both forms of a soliton packet, comparing the highest outlying mode to the adjacent mode energy at 150-Hz with a source depth of 60m. Mode 9 shows the greatest energy difference in decibels. Clearly mode 8 energy values are virtually indistinguishable between both shapes. The obvious difference between mode 9 values shows the sensitivity of shape to the phase at low energy modes. These modes, however can be ignored as their mode energy contributes almost	

	nothing to the entire acoustic pressure field. This is a similar result to the single soliton case.	33
Figure 18.	Parametric plot of mode energy for the sech^2 and Gaussian soliton packets; for 75, 150 and 300-Hz. The clear linear relationship demonstrates the validity of using a Gaussian shaped soliton in place of the sech^2 form.	34
Figure 19.	Relative mode energy $ A_n ^2/ A_{n0} ^2$ at 5km (averaged over the last 1000m) for a 75-Hz sound source and a source depth of 60m. This demonstrates a non-repeating mode pattern. Figure 20 shows the same plot with mode 2 removed to give a better perspective of the other modes.....	35
Figure 20.	Relative mode energy $ A_n ^2/ A_{n0} ^2$ at 5km (averaged over the last 1000m) for a 75-Hz sound source and a source depth of 60m. This plot excludes mode 2 to give a better perspective of the other modes. Again, this demonstrates a non-repeating mode pattern.	36
Figure 21.	Mode energy $ A_n ^2/ A_{n0} ^2$ at 5km (averaged over the last 1000m) for a 150-Hz sound source and a source depth of 60m. This demonstrates a non-repeating mode pattern.	37
Figure 22.	Mode energy $ A_n ^2/ A_{n0} ^2$ at 5km (averaged over the last 1000m) for a 300-Hz sound source and a source depth of 60m. This demonstrates a non-repeating mode pattern.	38
Figure 23.	Comparison of simulated (blue) and theoretical (green) results for a 75-Hz sound source at 60m, and a single wave moving between 1.5 and 3km. There is clearly very good agreement between the two results with almost identical mode pattern and virtually the same mode shape.	39
Figure 24.	Comparison of simulated (blue) and theoretical (green) results for the seven highest energy modes of a 150-Hz sound source at 60m, and a single wave moving between 1.5 and 3km. There is clearly very good agreement between the two results.	40
Figure 25.	Comparison of simulated (blue) and theoretical (green) results for the seven highest energy modes of a 300-Hz sound source at 60m, and a single wave moving between 1.5 and 3km. The similarity in both the mode pattern and mode energy is surprising at this relatively high frequency.....	41
Figure 26.	Parametric plot of simulated versus theoretical mode energies (for all modes) for a single soliton with a 60m source depth. The red line shows a linear relationship.....	43
Figure 27.	Parametric plot of simulated versus theoretical mode energies (for the seven highest energy modes) for a single soliton with a 60m source depth.	44
Figure 28.	Horizontal wavenumber versus node number, for all three frequencies, computed by the solution of the unperturbed mode equation (Equation 6)....	46
Figure 29.	Terms IV and VI of the modal evolution Equation (36). There is a clear linear increase of C_{mn} with frequency while D_{mn} shows vary little	

	variation with frequency. Together, these terms always act to increase the coupling strength with increasing frequency.	47
Figure 30.	The complex nature of the excitation energy shows that it can magnify or diminish the increase in mode coupling strength with frequency, caused by the terms C_{mn} and D_{mn}	47
Figure 31.	Allowable difference wavenumbers as a function of increasing frequency. The clear increase in allowable l_{mn} values with increasing frequency explains the increased granularity (or structure) observed with increasing frequency in Figures 19 to 22.	48
Figure 32.	Mode energy $ A_n ^2 / A_{n0} ^2$ at 5km (averaged over the last 1000m) for a wave packet with a 150-Hz sound source and a source depth of 60m. This demonstrates a non-repeating mode pattern.	49
Figure 33.	Comparison of simulated (blue) and theoretical (green) results for a 150-Hz sound source at 60m, and a wave packet moving between 1.5 and 3km (the same modes are compared as in the single wave case). There is clearly very good agreement between the two results; and the similarity in the pattern to the single wave case indicates that the first soliton is the most important in determining mode coupling at this frequency.	50
Figure 34.	Comparison of simulated (blue) and theoretical (green) results for a 300-Hz sound source at 60m, and a wave packet moving between 1.5 and 3km (the same modes are compared as in the single wave case). Again, the agreement between the two results in both the mode pattern and the mode energy is very good. The lack of variation in the wave pattern between the single wave case indicates that even at this frequency, the first wave in the packet dominates the coupling regime.	51
Figure 35.	Parametric plot of actual (simulated) versus theoretical mode energies (for all modes) for a wave packet with a 60m source depth.	52
Figure 36.	Parametric plot of actual (simulated) versus theoretical mode energies (for the seven modes compared in the single soliton case) for a wave packet with a 60m source depth.	53
Figure 37.	Comparison of simulated (blue) and theoretical (green) results for the seven highest energy modes of a 150-Hz sound source at 10m, and a single wave moving between 1.5 and 3km. There is clearly very good agreement between the two results.	54
Figure 38.	Parametric plot of actual (simulated) versus theoretical mode energies (for all modes) for a single soliton with a 10m source depth.	55
Figure 39.	Parametric plot of actual (simulated) versus theoretical mode energies (for the seven highest energy modes) for a single soliton with a 10m source depth.	56
Figure 40.	Parametric plot of actual (simulated) versus theoretical mode energies (for all modes) for a wave packet with a 10m source depth.	57
Figure 41.	Parametric plot of actual (simulated) versus theoretical mode energies (for the seven modes compared in the single soliton case) for a wave packet with a 10m source depth.	58

LIST OF TABLES

Table 1. Background sound speed parameters.....9

THIS PAGE INTENTIONALLY LEFT BLANK

ACKNOWLEDGMENTS

With most endeavors in life, the successes we obtain are often shaped by the contributions of other people. To that end, I would like to thank the following people, without whose help this project would have remained a pipe dream: To my thesis advisor John Colosi, your wisdom, guidance and instruction have been invaluable. I have thoroughly enjoyed working with you over the past nine months and have appreciated your patience with, and explanations to all of my questions—even the stupid ones.

From the NPS Meteorology and Oceanography departments: Special thanks goes to Mary Jordan for teaching me how to program. Without your expert instruction I wouldn't have made it past the introduction of this thesis. To Timour Radko, for bringing the subject of oceanography alive. To CDR Ben Reeder for setting me on the path of acoustics. And to LT Doug Roush: we shared in the same moments of confusion as well as enlightenment. I couldn't have asked for a better Lab partner.

From the Monterey community: Bill and Kathie Wilden, thanks for providing a home away from home. Your continual hospitality and friendship have made us feel like part of the family. Martin Densham and Gretta Spitz; your friendship will be cherished always.

From my family: Mum and Dad; from before I can remember you have encouraged me to achieve. Your example of life remains an inspiration to me. Raine Thompson, thank you for always cheering me on.

Most of all I would like to thank two very special people in my life: my beautiful daughter, Charlotte Grace, who has taught me what is most important in life; and my phenomenal wife Danielle. How can I ever express my gratitude for the unwavering love and support you have given me over the years? I love you.

THIS PAGE INTENTIONALLY LEFT BLANK

I. INTRODUCTION

In the oceanography community as a whole, internal solitary waves (ISW) have attracted great interest in recent times (Warn-Varnas et al., 1998). First noted by the engineer and ship builder John Scott Russell, in 1834, it was not until the 1960s that they were first studied in depth by Martin Kruskal and given the name “Solitons” (Weisstein, 2006a).

Although these waves can occur in the open ocean, they are common on the continental slope regions of the world (Preisig & Duda, 1997). They are often generated when tidal currents advect stratified water over the bathymetric relief, thus creating an internal tide which non-linearly evolves into one or more solitons. They appear as “propagating pulse-like depressions of the thermocline” (Preisig & Duda, 1997). A major consequence of solitons in a stratified environment is to vertically displace surface water to lower levels. This can have significant effects on temperature, salinity, density and therefore sound speed below the surface layer. Past studies have shown that, for frequencies of several hundred hertz, solitons can cause “erratic exchanges of acoustic energy between normal modes” (Duda & Preisig, 1999). In a study by Zhou, Zhang and Rogers (1991) acoustic fluctuations of order 20-40 dB were observed in the Yellow Sea. It is likely that these exchanges can cause significant variations in sonar performance on both surface based platforms and submarines.

In 1992 the United States Navy and Marine Corps white paper, entitled “From the Sea,” outlined the Navy’s strategic shift from an “open-ocean” focus toward the littoral zone. As a result of this shift, a significantly greater number of maritime exercises and operations are being conducted in regions which are commonly affected by solitons; hence an understanding into the nature of acoustic propagation and scattering through these waves is vital for future development of sonar prediction systems.

A. BACKGROUND

1. Shallow Water Acoustics and the Importance of Internal Solitary Waves

The growth in research into the effects of ISWs on acoustic propagation was sparked by the paper by Zhou et al. (1991); which hypothesized that large transmission

losses of order 20-40 dB that were observed in the Yellow Sea could be attributed to interactions with solitons (Shang, Wang & Ostrovsky 1998; Zhoe et al.). Subsequent experiments, such as the Shallow-Water Acoustic Random Media Experiment (SWARM), conducted in 1995, provided measured variability in the sound speed-field caused by the passage of internal solitary wave packets (Chiu,1998). In an attempt to better understand the causes of this large variability, a number of numerical simulations have been conducted. For shallow water problems, the most fruitful approach to understanding acoustic variability has been through the method of normal modes. The acoustic field at a particular frequency can be thought of as the sum of n propagating modes, with each mode carrying part of the energy of the wave. The energy distribution between modes is uneven such that for deep sources most energy tends to be in lower modes whilst for shallow sources the reverse is true. When an acoustic pressure wave makes contact with a soliton, the result is to redistribute the energy of the acoustic wave, among the various modes. This phenomenon of a particular mode losing energy to another, or alternatively, gaining energy from another, is termed mode coupling and the effects on the total acoustic field are for the amplitude and phase to fluctuate.

In 1997 Preisig and Duda investigated acoustic mode propagation through a single soliton using three different techniques. The first technique involved a wide-vertical-angled 2D parabolic equation method using a mode starting field and a standard sech^2 shaped soliton. The second approach approximated the soliton using the so called “sharp interface approximation” (SIA). This replaces the smooth sech^2 form with a boxcar shape, providing a useful method of analyzing mode coupling for small horizontal length scales. The third technique was based on an analytical derivation of the length scales which separate adiabatic and coupled mode propagation. The results from all three techniques showed that acoustic propagation through solitons resulted in mode coupling. The SIA technique explains some aspects of the coupling, based on both the spatial scale of the soliton and the modal phase, in three regimes. The first regime occurred for small scale solitons (less than 75m) which showed coupling to higher modes at the first interface of the soliton and an effective “uncoupling” at the second interface: the end result being no net mode coupling. The uncoupling phenomenon is called “cancellation” when the length scales are small but is termed “transparent resonance” for large length

scales (as the ISW is effectively transparent to the mode energy). The second regime, for soliton scales between 75 and 200m showed both coupling and transparent resonance. The dominant factor governing coupling in this region was the relative phase of the modes. The third regime for large scale ISWs showed predominately adiabatic propagation as “the horizontal gradients in the sound-speed profile are insufficient to induce coupling between acoustic modes” (Preisig & Duda, 1997). Naturally this third regime can not be approximated by the SIA technique as the very nature of a “Sudden Interface” describes a relatively sharp gradient.

In 1999 Preisig and Duda extended their study to include the more realistic case of a soliton wave packet with a 400-Hz sound source. Of primary importance in the study was the finding that wave packets close to a sound source, with most of the energy in the higher modes, caused a net coupling to lower order (hence lower attenuation) modes. This resulted in an amplification of acoustic energy at distant ranges. For a wave packet far from the sound source, the converse was true. Energy was coupled into even higher modes (Duda & Preisig, 1999).

2. Statement of Research

The objective of this paper is to examine acoustic normal mode propagation through solitons using a 2D parabolic equation simulation and weak acoustic scattering theory whose primary physics is a single scatter Bragg mechanism; as opposed to the SIA technique of Preisig and Duda (1997). This new theoretical approach is conceivably valid in all three of the regimes previously pointed out by Duda and Priesig. The theory will be tested against the simulation to determine if the total acoustic pressure field can be predicted in a soliton environment. A positive comparison between the theoretical results and the simulation could lead to the theory ultimately being incorporated in to sonar prediction software; providing increased accuracy in predicted acoustic ranges in littoral waters. The theory will be tested specifically in relation to acoustic frequency, soliton position with respect to the sound source and source depth. Frequencies of 75, 150 and 300-Hz will be examined, as well as source depths of 60m and 10m to cover the deep (submarine) and the shallow (surface ship) cases respectively. As it is more common for solitons to appear in a packet, rather than individually (Duda & Preisig, 1999), this paper will also examine mode coupling through soliton wave packets. Rather

than propagating individual modes, as done in previous research, this paper will focus on the more realistic case of a point source.

In addition to mode coupling, the shape of the soliton will be given consideration. Historically a hyperbolic secant form has been used to model solitons. This sech^2 wave form is used because the amplitude and horizontal displacement are solutions of the Korteweg de Vries (KdV) non linear wave equation which was first developed in 1895, 51 years after John Scott Russell first proposed the existence of solitary waves (Weisstein, 2006b). As a Gaussian shape is very similar to a hyperbolic secant, the Gaussian form may yield similar results with greater theoretical ease (Colosi, 2006). The difference between the two forms will be examined to determine if a Gaussian form can replace a sech^2 form for mathematical efficiency. The most appropriate form will be used in the comparison of the theory and the simulation. It is expected that the Gaussian approximation combined with weak acoustic scattering theory will allow for variations in both the spatial scale of the soliton and modal phase; therefore, a more realistic representation of mode coupling should be achievable compared to previous approximations, such as the boxcar or SIA method, whilst maintaining the benefits of these methods. The weak scattering theory presented in this thesis also points out the importance of Bragg scattering in acoustic / soliton interactions, a point that has not previously been appreciated.

Variations in the soliton structure will not be examined in this paper. A typical soliton profile has been chosen with length scale of 100m and amplitude of 10m.

II. METHODS OF ANALYSIS

A. PARABOLIC EQUATION METHOD

1. The Parabolic Equation

The parabolic equation method has become the most popular means of solving range dependent propagation problems since it was introduced into the field of underwater acoustics in 1973 by Hardin and Tappert (Jensen, Kuperman, Porter & Schmidt, 2000). This paper follows the derivation of the PE method given by Jensen et al.

The PE method begins with the Helmholtz equation which describes the development of acoustic pressure as a function of (in cylindrical coordinates) range (r), azimuth (φ) and depth (z). As with Jensen et al., azimuthal symmetry is assumed such that the φ -coordinate need not be considered. Hence, $p(r, z)$ is the acoustic pressure and the Helmholtz equation is thus,

$$\frac{\partial^2 p}{\partial r^2} + \frac{1}{r} \frac{\partial p}{\partial r} + \frac{\partial^2 p}{\partial z^2} + k_0^2 n^2 p \quad (1)$$

Where $k_0 = \frac{\omega}{c_0}$ is a reference wavenumber, $n(r, z) = \frac{c_0}{c(r, z)}$ is the index of refraction and $c(r, z) = \bar{c}(z) + \delta c(r, z)$. The solution to the Helmholtz equation is assumed to be of the form,

$$p(r, z) = \Psi(r, z) H_0^{(1)}(k_0 r) \quad (2)$$

Where $\Psi(r, z)$ is the wave envelope function and $H_0^{(1)}$ is a Hankel function of the first kind. Substituting this solution in to Equation (1) and making the small angle, or paraxial, approximation,

$$\frac{\partial^2 \Psi}{\partial r^2} \ll 2ik_0 \frac{\partial \Psi}{\partial r} \quad (3)$$

yields the standard parabolic equation, first introduced by Hardin and Tappert (Jensen et al, 2000):

$$2ik_0 \frac{\partial \Psi}{\partial r} + \frac{\partial^2 \Psi}{\partial z^2} + k_0^2 (n^2 - 1) \Psi = 0 \quad (4)$$

To analyze acoustic propagation it is often desirable to study modal behavior rather than the entire pressure field defined by the wave function $\Psi(r, z)$. The normal modes are extracted from the pressure field by first expanding the wave function in terms of the unperturbed modes (Colosi, 2006),

$$\Psi(r, z) = \sum_{n=1}^N A_n(r) \phi_n(z) \quad (5)$$

and

$$\left[\frac{\partial^2}{\partial z^2} - \bar{k}^2(z) - k_n^2 \right] \phi_n = 0, \quad \bar{k} = \frac{\omega}{c} \quad (6)$$

where $A_n(r)$ are the mode amplitudes and $\phi_n(z)$ are the unperturbed mode shapes. The mode amplitude can be obtained from the PE solution $\Psi(r, z)$ using,

$$A_m(r) = \int_0^D \Psi(r, z) \phi_m(z) dz \quad (7)$$

This result can be obtained by multiplying Equation (5) by the unperturbed modes ϕ_m and integrating from the surface to depth D . The quantity $A_m(r)$ will be our primary observable in the analysis of this thesis.

2. Boundary Conditions

In ocean acoustics it is customary to treat the surface as a reflecting, or pressure release, boundary; represented by the boundary condition $\Psi(r, 0) = 0$. This is easily dealt with in the PE method by the implementation of an image ocean. A second sound source is created in a reflected position above the ocean surface. By simply subtracting the input of the image source from that of the source at depth, the boundary condition is satisfied (Jensen et al., 2000):

$$\Psi(0, z) = \Psi(0, z - z_s) - \Psi(0, z + z_s) \quad (8)$$

where z_s is the source depth.

The bottom boundary is more complex and is treated by applying some form of attenuation function, or “sponge layer.” This is needed because the FFT solution (discussed later) has periodic boundary conditions. This means that a wave can exit the domain at the bottom and effectively re-enter the domain at the top if it is not attenuated via an absorption layer. To avoid this wrap-around-effect, a sponge layer used by Colosi and Flatté (1996) is reproduced for this paper:

$$L(z) = \exp \left\{ -\beta dx \times \exp \left[-\left(\frac{z - z_b}{\alpha z_b} \right)^2 \right] \right\} \quad (9)$$

where z_b is the bottom of the computational domain. The β term represents the relative strength of the loss and the α term represents where the loss is applied relative to the bottom. The chosen values of $\beta = 0.04$ and $\alpha = 0.05$ will stop acoustic energy from penetrating beyond 3.75m above 750m (10x the bottom of 75m); we do not model bottom attenuation.

3. Starting Field

An analytical starting field, in the form of a Gaussian point source is used to provide a realistic starting environment with little computational effort. The derivation in Jensen et al. yields the standard Gaussian point source used in this paper:

$$\Psi(0, z) = \sqrt{k_0} e^{-\frac{k_0}{2}(z-z_s)^2} \quad (10)$$

Where $\sqrt{k_0}$ is the effective source level and $\frac{k_0}{2}$ represents the beam width. Applying Equation (8) to take into account the surface boundary condition yields the starting field:

$$\Psi(0, z) = \sqrt{k_0} \left[e^{-\frac{k_0}{2}(z-z_s)^2} - e^{-\frac{k_0}{2}(z+z_s)^2} \right] \quad (11)$$

where k_0 can also be represented in terms of the initial frequency f_0 and the initial sound speed c_0 such that,

$$k_0 = \frac{2\pi f_0}{c_0} \quad (12)$$

4. Background Environment

The background environment is set up in three layers: A surface layer, a thermocline with a central depth of 30m, and an isovelocity profile below the thermocline to the bottom. A hyperbolic tangent function is used to transition the sound speed between the layers and the thermocline; and between the water column and the bottom. The use of a hyperbolic tangent function provides a more realistic ocean environment compared to a commonly used linear relationship, but provides less realistic transition at the ocean seabed interface. This smooth transition is required for the split-step method of the PE solution (more later). The total background sound speed is thus calculated as follows:

$$c = \left(c_s - \left| \frac{c_s - c_l}{2} \right| \right) \left(1 + \tanh \left[\frac{z - z_{th}}{\Delta_{th}} \right] \right) + \left| \frac{c_l - c_b}{2} \right| \left(1 + \tanh \left[\frac{z - (z_b + 4L)}{L} \right] \right) \quad (13)$$

where c_s is the surface sound speed, c_l is the lower layer sound speed, c_b is the sound speed in the bottom, z_{th} is the central depth of the thermocline, Δ_{th} is the width of the thermocline and L is a transitional length scale based on the acoustic wave length, such that $L = \frac{\lambda}{\pi}$.

Figure 1 shows the background sound speed profile used for this paper and Table 1 shows the values of the chosen parameters. For simplicity, the bottom has been modeled with sound speed only, thus a constant density of $1000(kg / m^3)$ has been used for the entire domain.

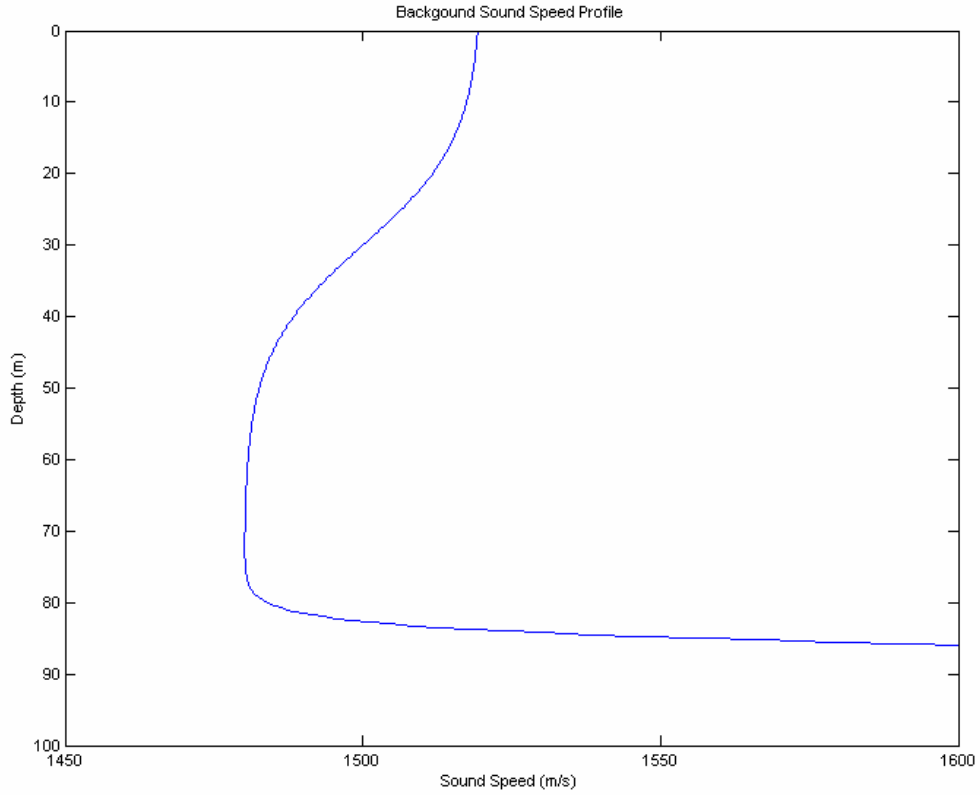


Figure 1. The background sound speed profile used in this study. The water column is divided into three layers and a hyperbolic tangent function is used to transition between the layers and the thermocline; and between the water column and the bottom.

Table 1. Background sound speed parameters

Surface sound speed c_s	1520 (m/s)
Lower layer sound speed c_l	1480 (m/s)
Bottom sound speed c_b	1980 (m/s)
Thermocline width Δ_{th}	15 (m)
Central depth of the thermocline z_{th}	30 (m)

5. Solutions to the Parabolic Equation Using the Split Step Fourier Algorithm

The Split Step Fourier method for solving the PE problem, introduced by Hardin and Tappert, has since become one of the most widely used methods in underwater acoustics (Jensen et al., 2000). The advantages and disadvantages of this method, as well as the derivation have been covered sufficiently in other texts and will not be covered here. This paper uses the following form of the Split Step Fourier Algorithm (Jensen et al 2006):

$$\Psi(r, z) = F^{-1} \left\{ e^{-\frac{i\Delta r}{2k_0} k_z^2} F \left\{ e^{\frac{ik_0}{2} [n^2(r_0, z) - 1] \Delta r} \Psi(r_0, z) \right\} \right\} \quad (14)$$

The Split step algorithm is so called because it first marches the solution out in range using a phase screen which takes refractive effects into account. It then advances the solution for a homogeneous medium to include diffraction (other forms of the algorithm produced by Jensen et al., consider the homogeneous solution first).

To test the stability of the PE code, the model was run using a point source in the background sound speed environment (no soliton). In this case there should be no mode coupling and the magnitude of the mode amplitudes $|A_n|$ should be independent of r . The source was set at a depth of 60m, and the code was run at 75, 150 and 300-Hz respectively to a range of 5km. Figure 2 shows the entire acoustic field to a depth of 200m (noting the bottom is at 75m). Figures 3, 4 and 5 show the mode energy $|A_n|^2(r)$ (lower panel) and the fluctuation, or variance, of mode energy (upper panel). For frequencies of 75, 150 and 300-Hz there are 7, 12, and 20 trapped modes respectively, and for all these trapped modes, which carry all the energy, the fluctuation in mode energy is very small. Thus the code is quite stable for all of the frequencies trialed.

B. SOLITARY WAVE MODELING

1. Single Soliton

The solitary wave is incorporated into the PE model by producing a perturbation in the background sound speed. The hyperbolic secant form of the soliton is a solution to the KDV wave equation. After making the frozen field approximation, the soliton can be represented by the following mathematical representation:

$$\zeta(r, z) = B(z) \sec h^2 \left(\frac{r - r_0}{\Delta_s} \right) \quad (15)$$

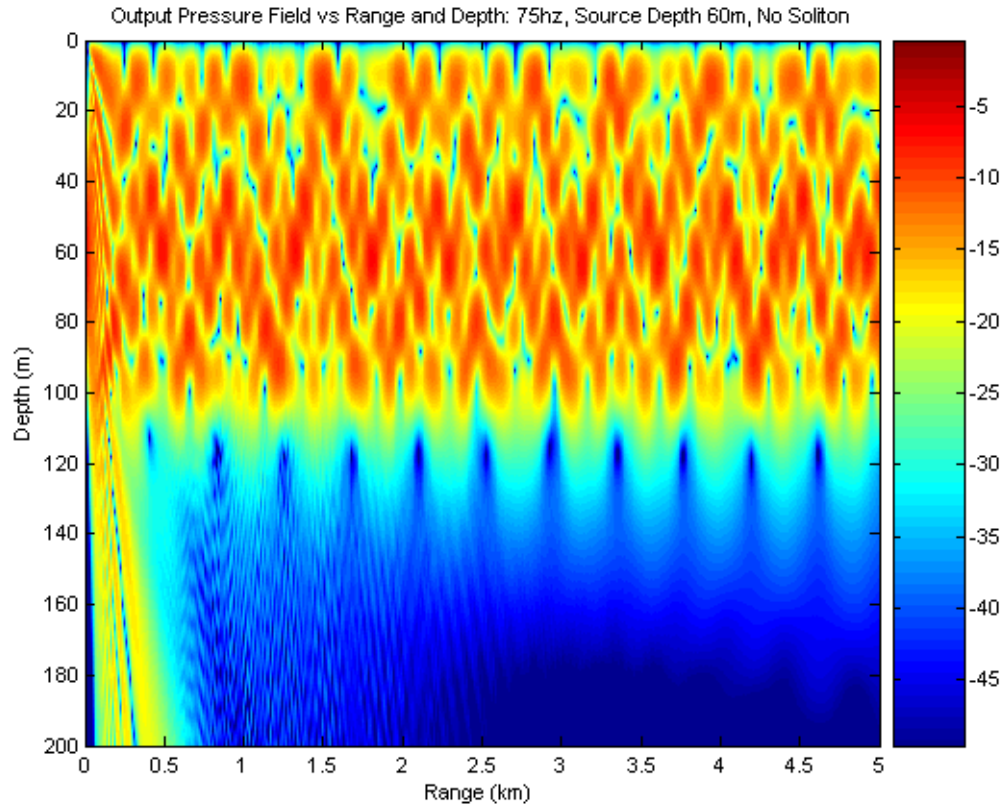


Figure 2. Simulation of the total acoustic pressure field in decibels for a 75-Hz source at 60m.

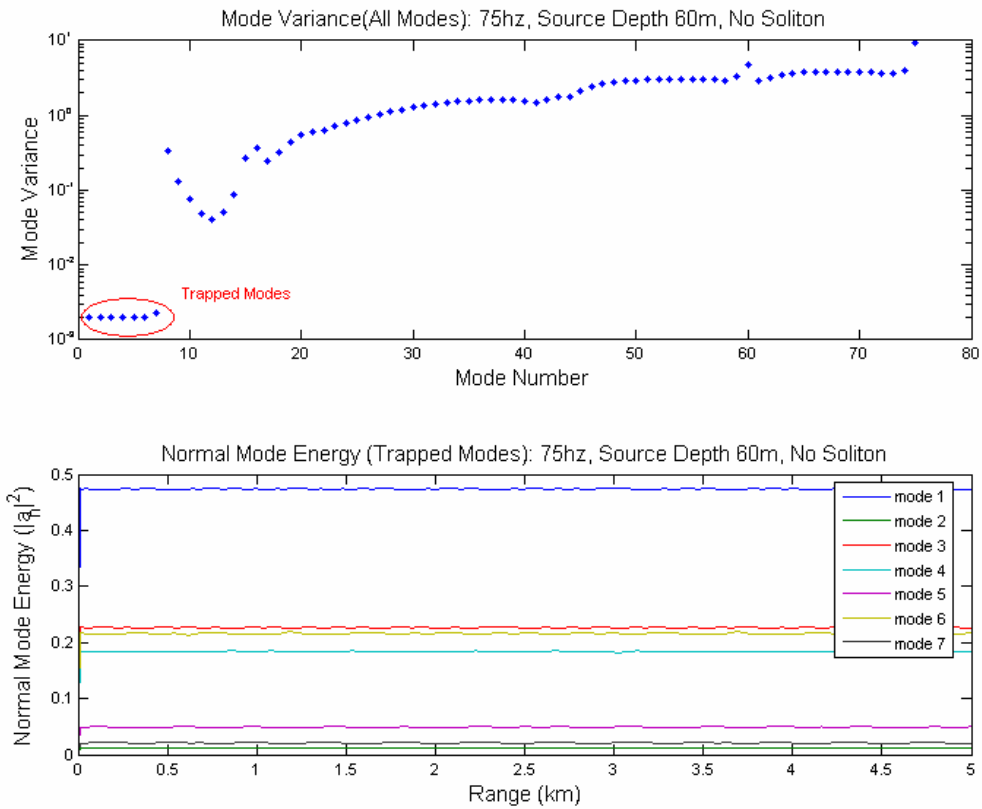


Figure 3. To test mode energy conservation, the model is run with just the background sound speed environment, a frequency of 75-Hz and a source depth of 60m. The first plot shows the mode variance for each mode with only the first 7 modes being trapped. The mode energies $|A_n|^2(r)$ are represented in the second plot.

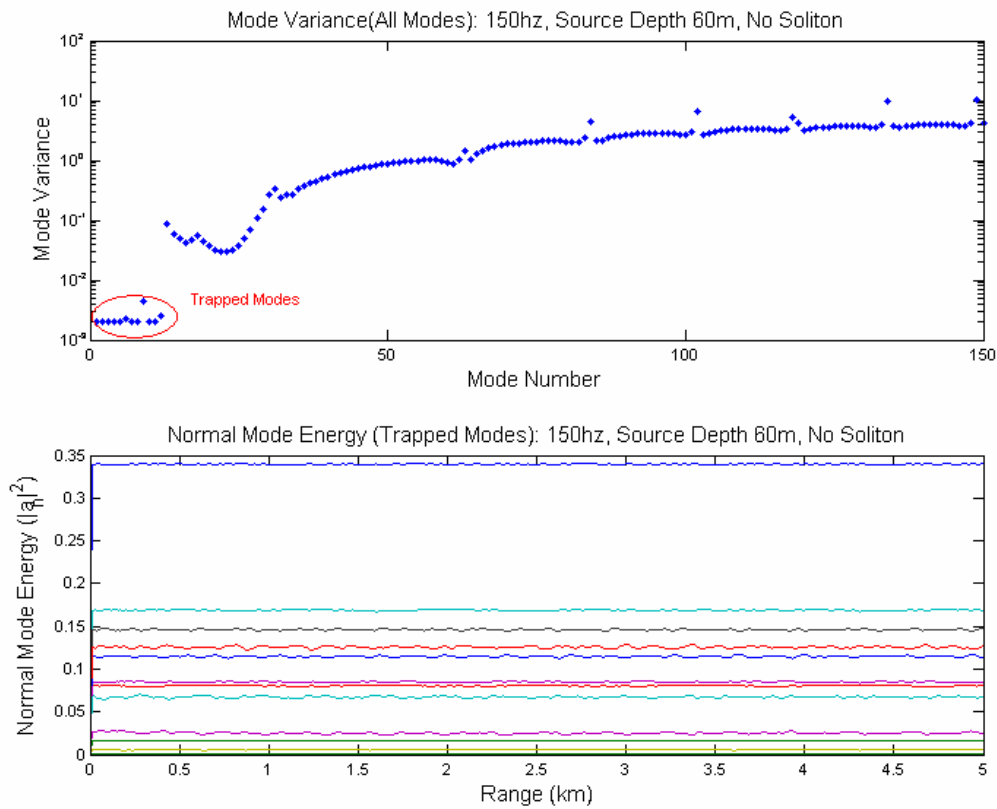


Figure 4. To test mode energy conservation, the model is run with just the background sound speed environment, a frequency of 150-Hz and a source depth of 60m. The first plot shows the mode variance for each mode with only the first 12 modes being trapped. The mode energies $|A_n|^2(r)$ are represented in the second plot.

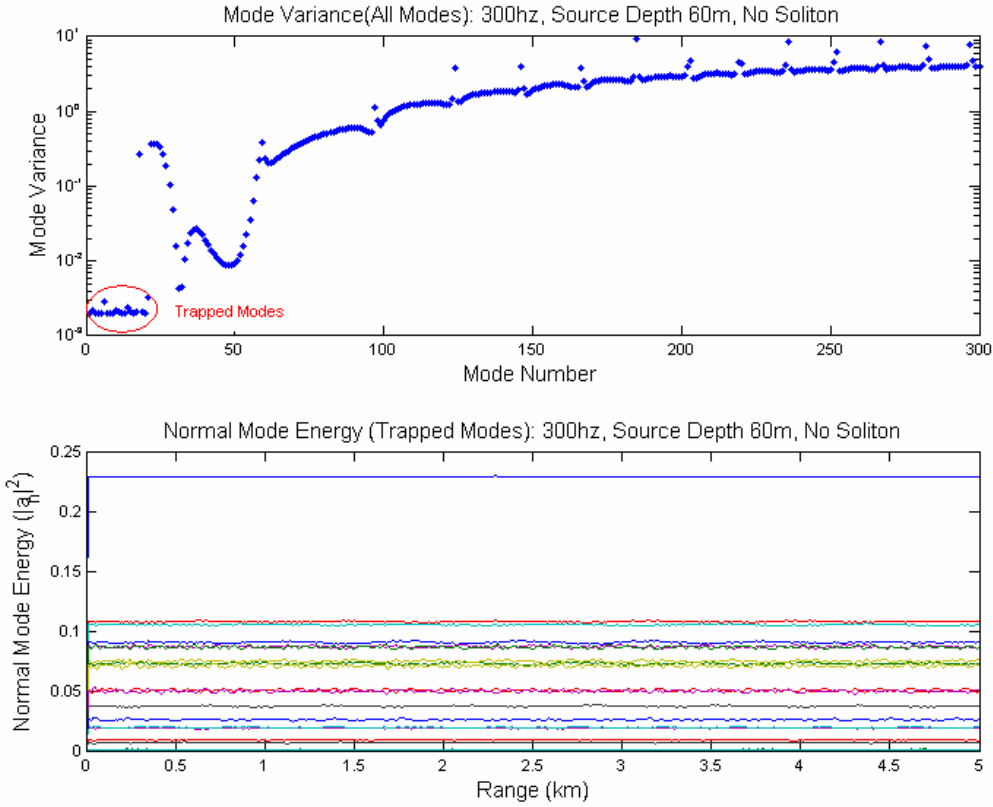


Figure 5. To test mode energy conservation, the model is run with just the background sound speed environment, a frequency of 300-Hz and a source depth of 60m. The first plot shows the mode variance for each mode with only the first 20 modes being trapped. The mode energies $|A_n|^2(r)$ are represented in the second plot.

where the sech^2 function represents the soliton shape, r_0 is the soliton central location, Δ_s is the soliton width; and the amplitude $B(z)$ is the depth structure of the soliton which should approximate a sinusoidal form such as $\zeta_0 \sin\left(\frac{\pi z}{D}\right)$, where ζ_0 is the maximum amplitude of the soliton. To limit the sinusoidal function influence to the water column, a hyperbolic tangent function is again used to transition from the soliton to the background environment. Figure 6 demonstrates the effect of applying the hyperbolic tangent function to the soliton amplitude. The total soliton is thus represented by:

$$\zeta(r, z) = \zeta_0 \sin\left(\frac{\pi z}{D}\right) \left\{ 1 - \frac{1}{2} \left(1 + \tanh \left[2 \left(\frac{z - (D - L)}{L} \right) \right] \right) \right\} \operatorname{sech}^2 \left(\frac{r - r_0}{\Delta_s} \right) \quad (16)$$

The perturbed sound speed profile can now be calculated using the relationship,

$$c(z + \zeta) = c(z) + \frac{\partial c}{\partial z} \zeta(r, z) \quad (17)$$

Figure 7 shows the total sound speed field for a single soliton of width 100m, maximum amplitude of 10m, at a range of 2.5km from the intended sound source.

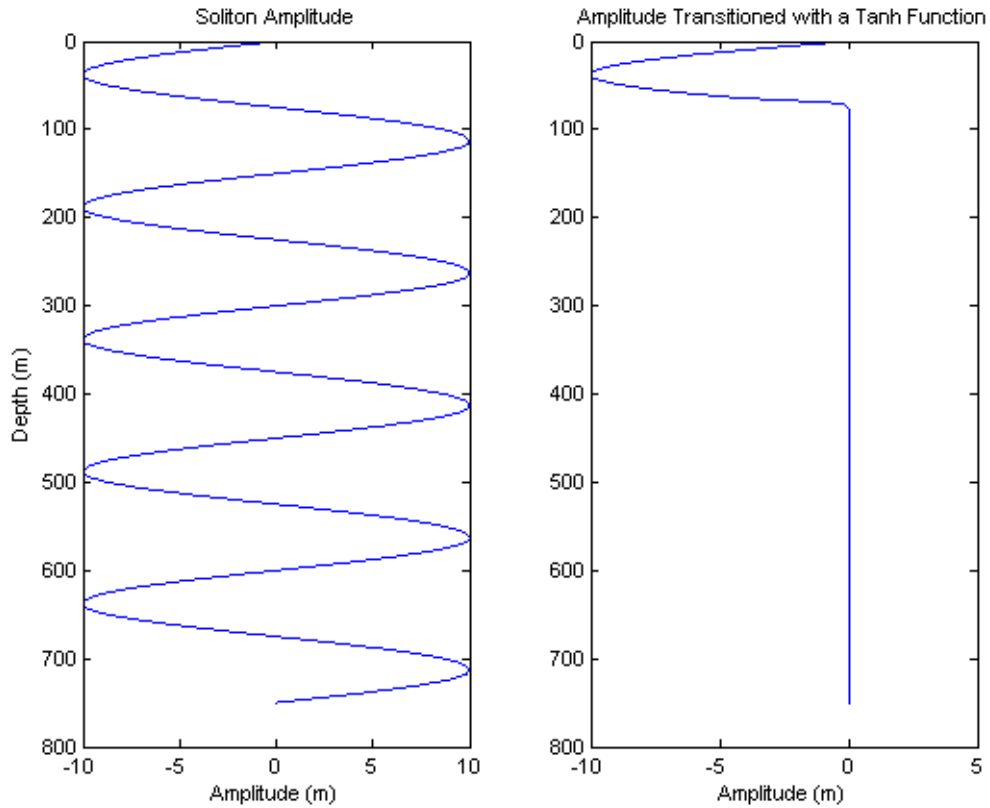


Figure 6. A hyperbolic tangent function is used to transition the soliton amplitude to the background environment.

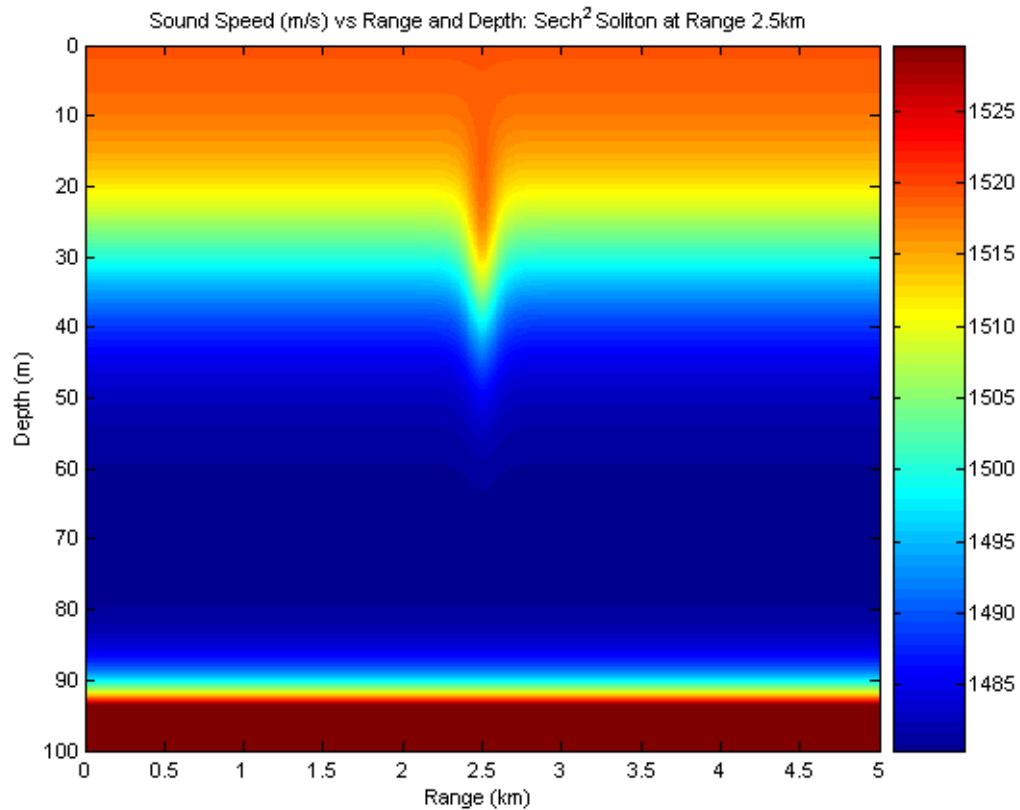


Figure 7. Total sound speed field with a sech^2 shaped soliton at a range of 2.5km. The soliton width is 100m and the maximum amplitude is 10m.

2. Soliton Wave Packet

Solitons tend to appear in the environment as a wave packet rather than individually (Duda & Preisig, 1999). To consider this more realistic scenario, a wave packet is created in the same manner as a single soliton. The total sound speed field is simply the background sound speed plus the perturbation contribution made by each wave in the packet. Figure 8 shows a typical soliton wave packet with each consecutive soliton decreasing in amplitude. The soliton widths have been kept constant at 100m and they are each separated by 500m.

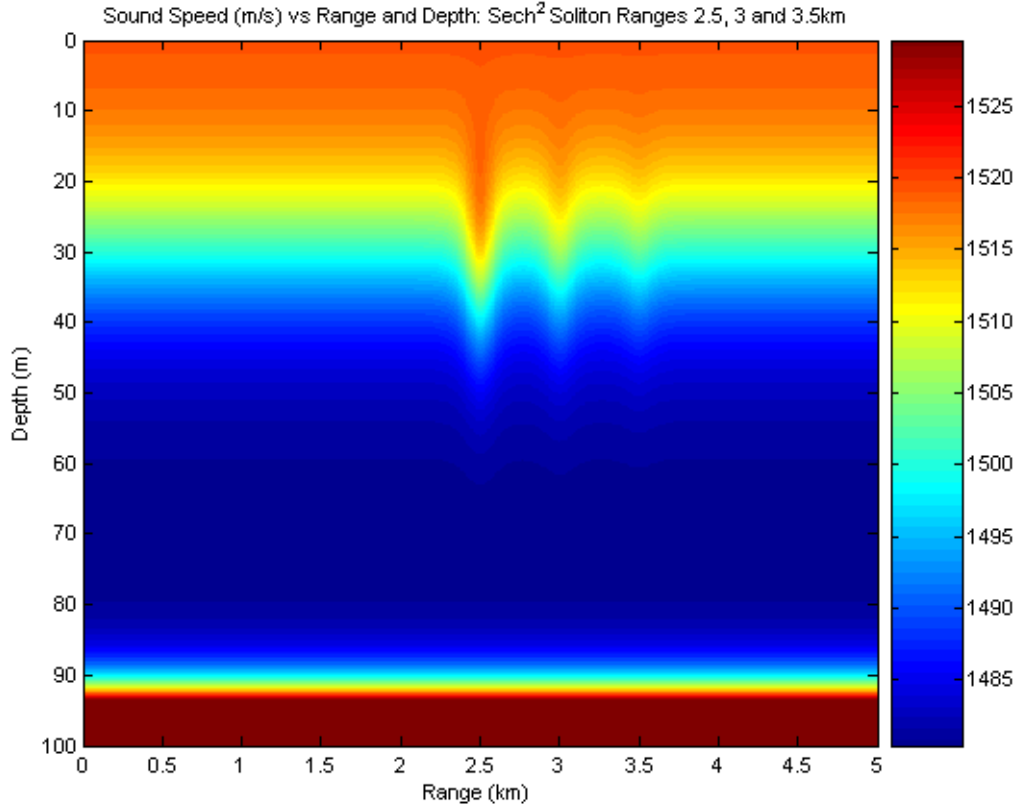


Figure 8. Total sound speed field with a sech^2 shaped soliton wave packet. The solitons are at ranges of 2.5, 3 and 3.5km and have constant width of 100m. The maximum amplitudes are 10, 5 and 2.5m respectively.

C. THE PARABOLIC EQUATION IN MODE FORM

As this paper focuses primarily on mode coupling, it is useful to express the parabolic equation in mode form. The following derivation follows directly from Colosi 2006. Equations (5), (6) and (7) lead to an equation for mode amplitude in the form,

$$\left[\frac{\partial}{\partial r} - i \frac{k_n^2 - k_0^2}{2k_0} \right] A_n = \frac{i}{2k_0} \sum_{m=1}^N C_{mn} A_m \quad (18)$$

where C_{mn} is the random mode coupling matrix defined by,

$$C_{mn} = \int_0^D (k^2(r, z) - \bar{k}^2(z)) \phi_n \phi_m dz \approx -2k_0^2 \int_0^D \mu(r, z) \phi_n \phi_m dz \quad (19)$$

and $\mu = \frac{\delta c}{c_0}$. To simplify the notation, Equation (18) becomes,

$$\left[\frac{\partial}{\partial r} - i \frac{k_n^2 - k_0^2}{2k_0} \right] A_n = -i \sum_{m=1}^N \rho_{mn} A_m \quad (20)$$

$$\rho_{mn}(r) = k_0 \int_0^D \mu(r, z) \phi_n \phi_m dz \quad (21)$$

Equation (20) can be simplified further by using the following definitions:

$$\psi_n = A_n \exp(-il_n r), \quad l_n = \frac{k_n^2 - k_0^2}{2k_0} \quad (22)$$

which gives the acoustic wave equation in mode form (an exact representation of Equation (4)):

$$\frac{\partial \psi_n}{\partial r} = -i \sum_{m=1}^N \rho_{mn} e^{il_{mn} r} \psi_m, \quad l_{mn} = l_m - l_n = \frac{k_m^2 - k_n^2}{2k_0} \quad (23)$$

1. Perturbation Theory

Perturbation theory provides a useful method of analyzing the environmental effects on individual modes. Again, from Colosi (2006), Equation (23) can be written as a series solution as long as ρ_{mn} is sufficiently small (of the order ε):

$$\frac{\partial}{\partial r} (\psi_{n0} + \psi_{n1} + \psi_{n2} \dots) = -i \sum_{m=1}^N \rho_{mn} e^{il_{mn} r} (\psi_{m0} + \psi_{m1} + \psi_{m2} \dots) \quad (24)$$

where $\psi_{n0}, \psi_{n1}, \psi_{n2} \dots$ etc are of the order $\varepsilon^0, \varepsilon^1, \varepsilon^2, \dots$ etc. From this, it follows that

$$\begin{aligned} \frac{\partial}{\partial r} \psi_0 &= 0 \\ \frac{\partial}{\partial r} \psi_{n1} &= -i \sum_{m=1}^N \rho_{mn}(r) e^{il_{mn} r} \psi_{m0}(r) \\ &\vdots \\ \frac{\partial}{\partial r} \psi_{nj} &= -i \sum_{m=1}^N \rho_{mn}(r) e^{il_{mn} r} \psi_{mj-1}(r) \end{aligned} \quad (25)$$

with initial conditions, $\psi_n(0) = \psi_{n0}, \psi_{n1}(0) = \psi_{n2}(0) = \dots = 0$. A solution is constructed to any order of ε , so that

$$\begin{aligned}
\psi_0(R) &= \psi_{n0}(0) = \psi_n(0) \\
\psi_{n1}(R) &= -i \sum_{m=1}^N \psi_m(0) \int_0^R dr' \rho_{mn}(r') e^{il_{mn}r'} \\
&\vdots
\end{aligned} \tag{26}$$

where R is the final range, on the other side of the soliton. For simplicity, the first order perturbation solution is,

$$\psi_n(R) = \psi_n(0) - i \sum_{m=1}^N \psi_m(0) \int_0^R dr' \rho_{mn}(r') e^{il_{mn}r'} \tag{27}$$

Finally, using the spectral notation,

$$\rho_{mn}(r) = \int_{-\infty}^{\infty} dk \hat{\rho}(k) e^{-ikr}, \quad \hat{\rho}_{mn}(k) = \frac{1}{2\pi} \int_{-\infty}^{\infty} dr \hat{\rho}_{mn}(r) e^{-ikr} \tag{28}$$

the perturbation solution is,

$$\psi_n(R) = \psi_n(0) - i \sum_{m=1}^N \int dk \hat{\rho}_{mn}(k) \psi_m(0) \int_0^R dr' e^{i(l_{mn}-k)r'} \tag{29}$$

2. Sound Through Solitons

The more general form for ocean solitons (combining Equations 16 and 17) can be expressed as,

$$\mu(r, z) = \mu_0 W_1(z) F(r) \tag{30}$$

such that the mode coupling coefficients become

$$\rho_{mn} = k_0 \int_0^D \phi_n(z) \mu(r, z) \phi_m(z) dz = C_{mn} F(r) \tag{31}$$

Equation (29) (the modal evolution equation) is re-written as

$$\psi_n(R) = \psi_n(0) - i \sum_{m=1}^N \psi_m(0) \int dk \hat{\rho}_{mn}(k) \psi_m(0) H_{mn}(R, k) \tag{32}$$

The last integral in Equation (29), H_{mn} has the form

$$\begin{aligned}
H_{mn}(R, k) &= \int_0^R dr' e^{i(l_{mn}-k)r'} \\
&= R e^{i(l_{mn}-k)(R/2)} \operatorname{sinc} \left[(l_{mn}-k) \frac{R}{2} \right] \approx 2\pi \delta(l_{mn}-k). \quad (33)
\end{aligned}$$

where the last step follows for large R . This delta function reveals the Bragg scattering condition in which the solitary wavenumber, which resonates with the beat wavenumber between the modes n and m , provides the important scattering.

3. The Gaussian Soliton

As discussed, the sech^2 form of a soliton is chosen because it is an exact solution to the KDV wave equation. For analytical efficiency it is convenient to approximate the sech^2 soliton with a Gaussian form (see Figure 9) such that,

$$F(r) = \operatorname{sech}^2 \left[\frac{(r-r_0)}{\Delta_s} \right] \approx \exp \left[-\frac{(r-r_0)^2}{\Delta_s^2} \right] \quad (34)$$

The mode coupling coefficients can then be written as,

$$\begin{aligned}
\hat{\rho}_{mn}(k) &= \frac{1}{2\pi} C_{mn} \int_{-\infty}^{\infty} \exp \left[-\frac{(r-r_0)^2}{\Delta_s^2} \right] e^{ikr} dr \\
&= \frac{\Delta_s}{2\sqrt{\pi}} C_{mn} e^{ik\bar{r}} \exp \left[-\frac{k^2 \Delta_s^2}{4} \right] \quad (35)
\end{aligned}$$

The first order result of the modal evolution Equation (32) can now be expressed as,

$$\begin{aligned}
\psi_n(R) &= \psi_n(0) - i\Delta_s \pi^{1/2} \sum_{m=1}^N \psi_m(0) C_{mn} e^{i l_{mn} r_0} \exp \left[-\frac{l_{mn}^2 \Delta_s^2}{4} \right] \\
&\dots I \dots \dots \dots II \dots \dots \dots III \dots IV \dots V \dots \dots \dots VI \dots
\end{aligned} \quad (36)$$

This appears to be a very useful approximation as all relevant characteristics of the soliton are included in the modal evolution equation. Term *I* represents the complex mode amplitude after it has passed through the soliton. Term *II* represents the initial mode amplitude. Term *III* represents the contributions made to the initial mode n , by other m modes as it passes through the soliton. Term *IV* is the random mode coupling matrix dependent on the vertical structure of the modes and the soliton. Term *V* is a

phase term which depends on the central position of the soliton; and the final term, VI , represents both the mode number difference l_{mn}^2 and the width of the soliton Δ_s .

Terms V and VI constitute what is known as the Bragg condition. From the theory it can be seen that certain wavenumbers in the soliton resonate with the “beat” wavenumber (k_{beat}) of the modes (Equation 33). The beat wavenumber has special physical meaning and is the spatial frequency of the envelope of the interference pattern of two superposed waves. $2\pi/k_{beat}$ can also be represented as a ray cycle distance. Thus the meaningful quantity for the soliton to resonate with is the beat wavenumber. This resonance can be related to the well known Bragg resonance which is usually expressed in terms of spatial dimensions instead of wavenumbers. The traditional Bragg condition for scattering from a molecular lattice says that the strongest backscatter occurs when an integer number of wavelengths can fit between the Bragg planes of the lattice; for simple solids and at normal incidence the distance between Bragg planes is just the intermolecular distance d ; thus the expression $n\lambda = 2d$. For our condition we have $2\pi/d_{soliton} = 2\pi/\lambda_{beat}$ or $\lambda_{beat} = d_{soliton}$. Essentially the width of the soliton is analogous to the molecular lattice spacing, thus first order theory deals with acoustic wavelengths which are equal to the soliton width. Naturally a higher order theory would allow for multiple wavelengths to fit within the width of the soliton. This paper only deals with first order theory.

Physically Equation (36) is a single scatter model; mode n couples to mode m with no intermediated state. It should be noted that in evaluating H_{mn} , it is assumed that R is very large and that both the initial point $r = 0$ and the final range R are well away from the soliton. As this paper deals primarily with absolute mode energy, rather than individual mode amplitudes, we square Equation (36) and convert to the A_n representation (Equation 22) to obtain the mode energy equation to first order

$$|A_n(R)|^2 = |A_n(0)|^2 + 2\Delta_s \pi^{1/2} \sum_{m=1}^N A_m(0)A_n(0)C_{mn} \exp\left[-\frac{l_{mn}^2 \Delta_s^2}{4}\right] \sin(l_{mn}r_0). \quad (37)$$

Since in this research we are examining relative mode energy change, we also have

$$\frac{|A_n(R)|^2}{|A_n(0)|^2} = 1 + 2\Delta_s \pi^{1/2} \sum_{m=1}^N \frac{A_m(0)A_n(0)}{|A_n(0)|^2} C_{mn} \exp\left[-\frac{l_{mn}^2 \Delta_s^2}{4}\right] \sin(l_{mn} r_0). \quad (38)$$

As this thesis also examines the more realistic case of a soliton packet, we can use the linearity of the Fourier transform to obtain the modal evolution equation for the packet:

$$\psi_n(R) = \psi_n(0) - i\Delta_s \pi^{1/2} \sum_{k=1}^{N_s} \Delta_s(k) \sum_{m=1}^N \psi_m(0) C_{mn}(k) e^{i l_{mn} r_0(k)} \exp\left[-\frac{l_{mn}^2 \Delta_s^2(k)}{4}\right] \quad (39)$$

Where N_s is the number of solitons in the packet, and $\Delta_s(k)$, $r_0(k)$, and $C_{mn}(k)$ are the width, position, and coupling matrix of the k^{th} soliton. Thus the first order mode energy equation for the wave packet case can be written as

$$|A_n(R)|^2 = |A_n(0)|^2 + 2\Delta_s \pi^{1/2} \sum_{k=1}^{N_s} \Delta_s(k) \sum_{m=1}^N A_m(0)A_n(0) C_{mn}(k) \exp\left[-\frac{l_{mn}^2 \Delta_s^2(k)}{4}\right] \sin(l_{mn} r_0(k)) \quad (40)$$

Figure 9 shows a comparison between the sech^2 and the Gaussian shapes, both with relative amplitudes of 1, at an arbitrary distance. Both of these forms have been incorporated into the PE model. In a similar manner to Equation (16), the Gaussian soliton is represented by,

$$\zeta(r, z) = \zeta_0 \sin\left(\frac{\pi z}{D}\right) \left\{ 1 - \frac{1}{2} \left(1 + \tanh \left[2 \left(\frac{z - (D-L)}{L} \right) \right] \right) \right\} \exp\left(-\frac{(r-r_0)^2}{\Delta_s^2}\right) \quad (41)$$

A comparison is made between the outputs of trapped modes for each shape with the results discussed in the next chapter.

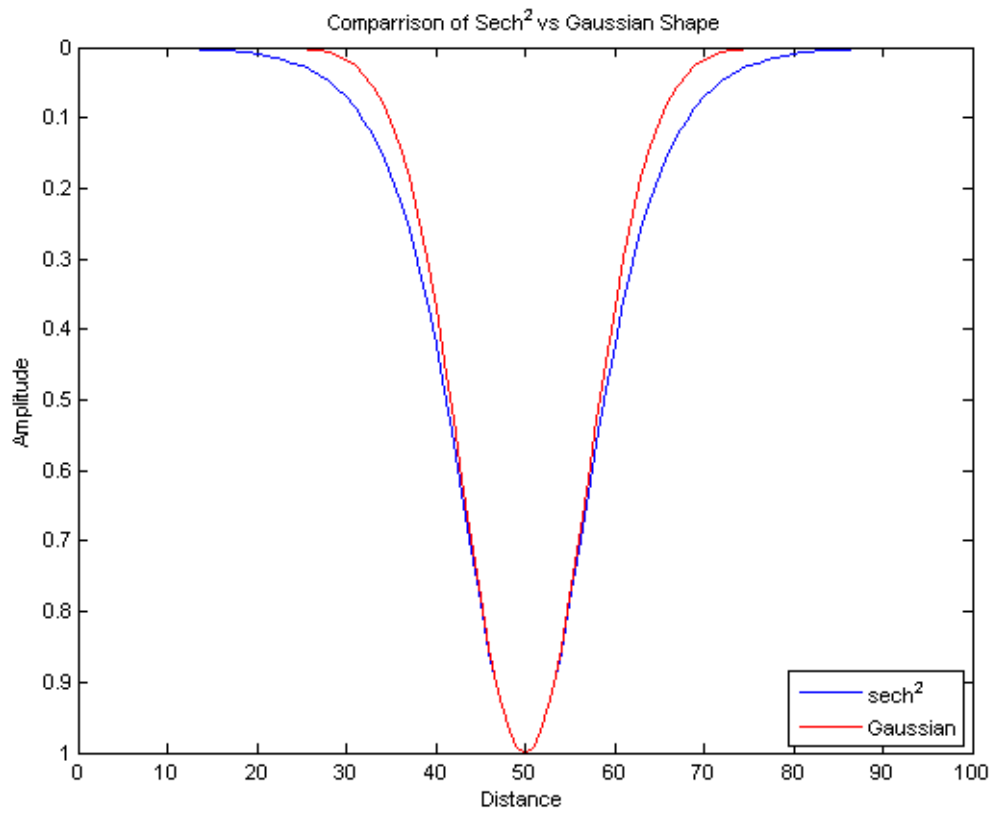


Figure 9. A comparison of the sech^2 and Gaussian wave forms.

THIS PAGE INTENTIONALLY LEFT BLANK

III. RESULTS

A. SECH² VERSUS GAUSSIAN SOLITON

1. Single Wave

The model was run with both soliton forms and a comparison was made using the mode energies, $|A_n|^2(r)$. Only trapped modes are examined in the analyses for this thesis. These correspond to modes 1-7 for 75-Hz, modes 1-12 for 150-Hz and modes 1-20 for 300-Hz and the trapped modes represent the dominant acoustic energy excited by the source. Figure 10 shows an overlay of mode energy output for a point source at frequency of 150-Hz, depth of 60m and a soliton range of 2.5km. Clearly there is very little difference between the final mode energy for both soliton models. Similar results were obtained for a point source at 75 and 300-Hz.

A plot of mode energy difference was then constructed. Because of small numerical fluctuations in mode energy with range we averaged the mode energy for the last 1000m at the range, to get a single mode energy estimate $|A_n|^2(r)$ after the soliton. Dividing this energy value by the initial mode energy and taking the log gives us the fractional energy change in dB. This plot appears at Figure 11 but on initial inspection it appears that several modes display significant variation between the two wave shapes; for example, mode 9 at 150-Hz and mode 18 at 300-Hz. To resolve this issue plots were constructed of the mode energy for these large deviation cases (mode 9 at 150-Hz and mode 18 at 300-Hz) compared to the neighboring mode energy. Figure 12 shows modes 1 and 2 for a 75-Hz source (where mode 2 has a large deviation). Figure 13 is a plot of modes 8 and 9 for a 150-Hz source and Figure 14 is a plot of modes 17 and 18 for a 300-Hz source. For each case it is clear that for modes with sufficient energy, very little difference is seen between the sech² and Gaussian solitons. The modes which show significant difference are those with small energy values. Clearly by calculating the logarithmic difference of two very small numbers, a relatively large number can occur. Low energy modes are very sensitive to the phase of the mode in relation to the soliton but as their energy contributes virtually nothing to the acoustic pressure field, they can be ignored.

A parametric plot of $|A_n|^2(r)$ for the Gaussian versus $|A_n|^2(r)$ for the sech^2 was created for each frequency and is shown at Figure 15. There is a clear linear relation exhibited in all three cases which further support that a Gaussian model provides a very good approximation to the sech^2 form of the soliton for a single wave.

Both shapes were also run with a soliton at 1.5km from the source with the same source depth and then at 2.5km with a source depth of 50m. By moving the soliton closer the same modes are affected however, the values differ. By changing the source depth there is a different distribution of mode energy. For each case the comparisons made reflected the results previously discussed.

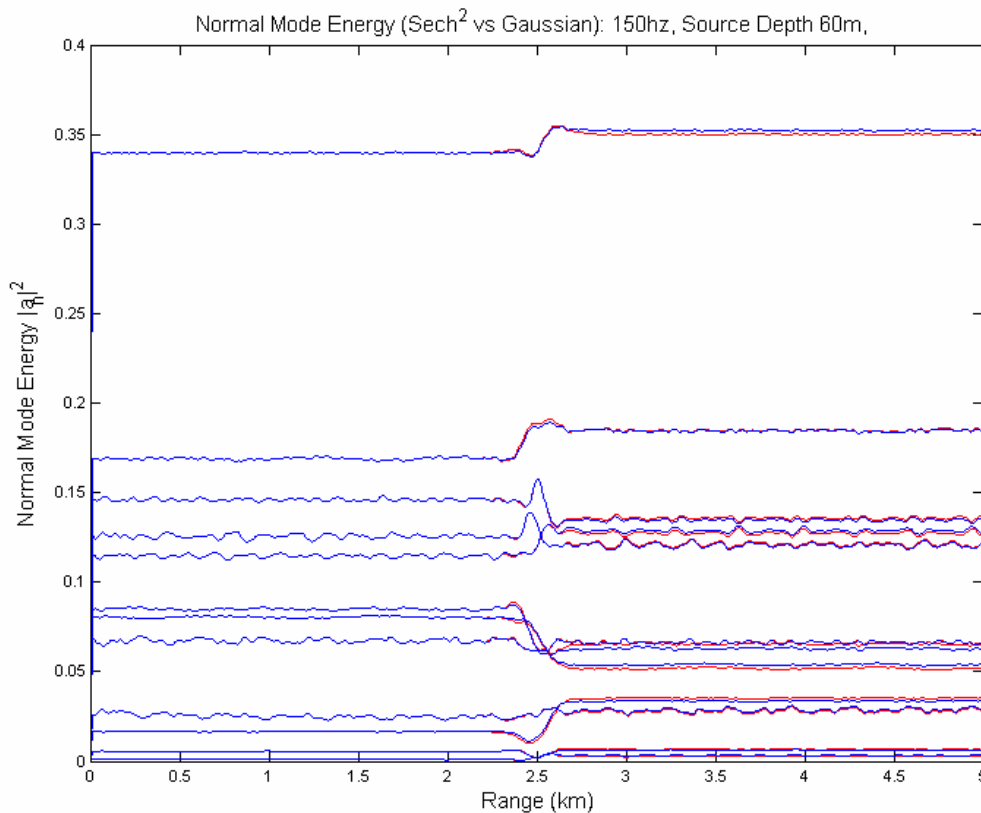


Figure 10. Mode energy $|A_n|^2(r)$ comparison between a sech^2 (red) and a Gaussian (blue) soliton shape for a single wave with a source depth of 60m and a frequency of 150-Hz. Similar results appear for all three frequencies. By visual inspection there is very little difference between the two shapes.

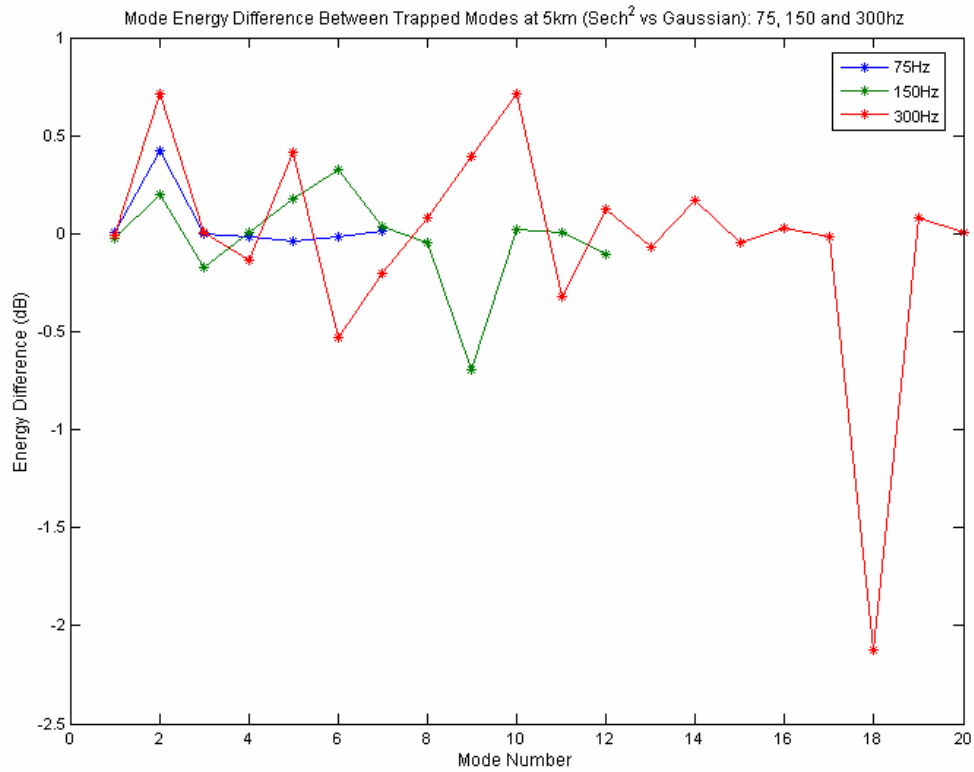


Figure 11. Relative mode energy $10\log_{10}\left(\frac{|A_n|^2}{|A_{n0}|^2}\right)$ between trapped modes for a single soliton, for all three frequencies at a range of 5km. The soliton is located at 2.5km. These results were obtained from averaging the mode energy of the last 1000m and comparing the difference between the two shapes in logarithmic form. The values which are not close to zero (e.g. mode 9 at 150-Hz and mode 18 at 300-Hz) are discussed in Figures 12 to 14.

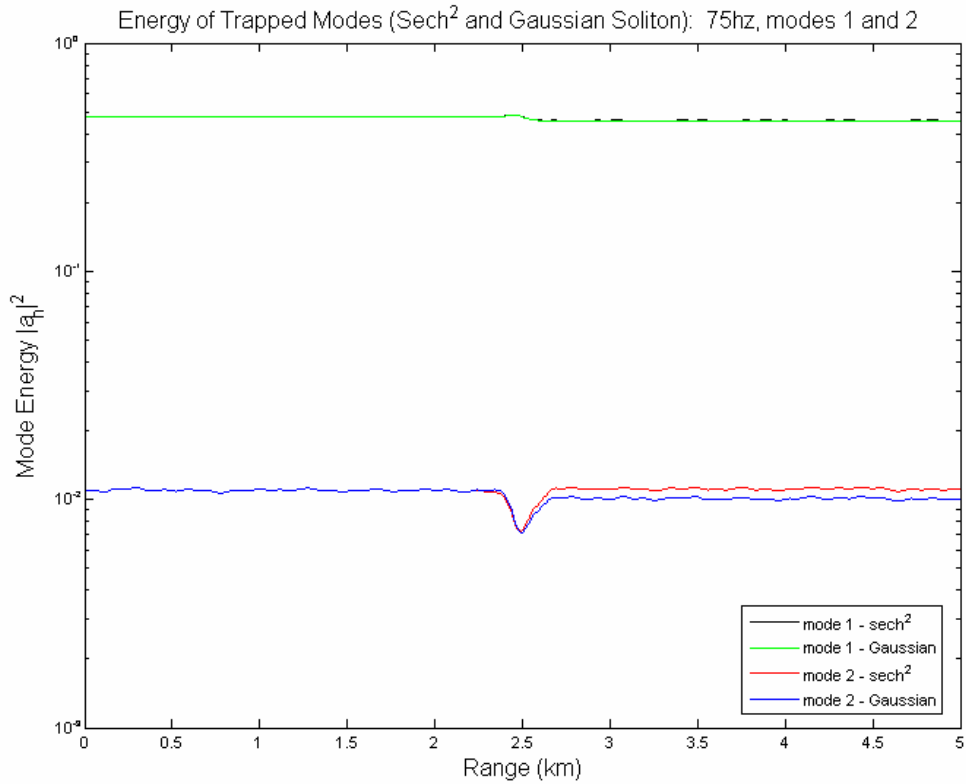


Figure 12. Mode energy $|A_n|^2(r)$ of a single soliton for both soliton forms, comparing the highest outlying mode to the adjacent mode energy at 75-Hz with a source depth of 60m. Mode 2 showed the greatest energy difference in decibels. Clearly mode 1 energy values are virtually indistinguishable between both shapes. The obvious difference between mode 2 values shows the sensitivity of shape to the phase at low energy modes. These modes, however can be ignored as their mode energy contributes almost nothing to the entire acoustic pressure field.

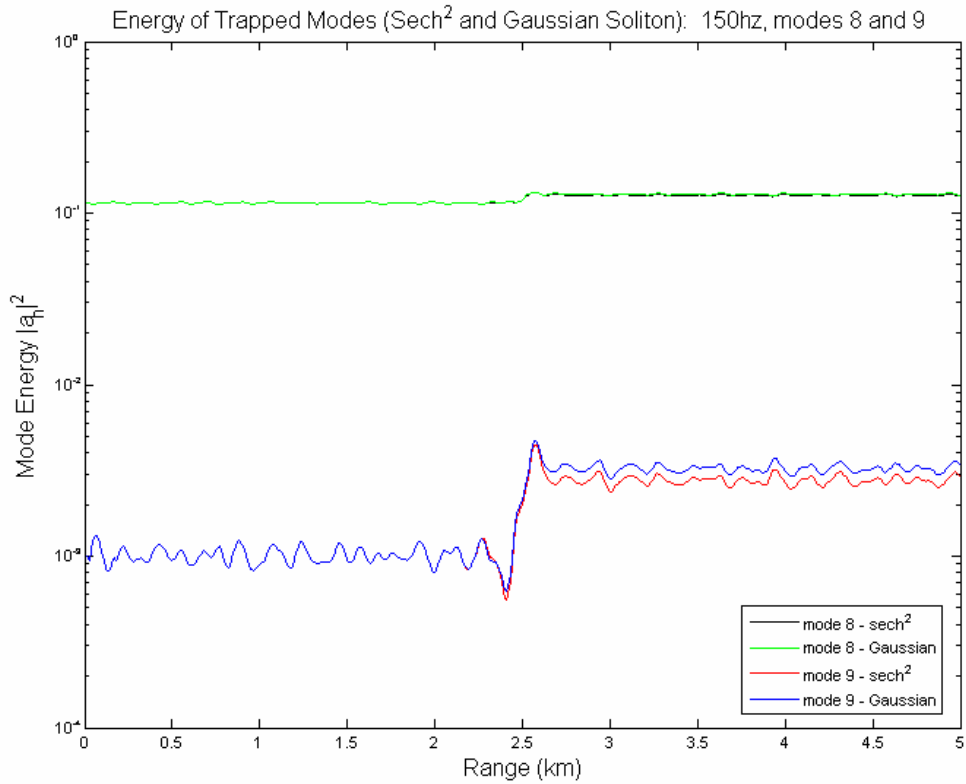


Figure 13. Mode energy $|A_n|^2(r)$ of a single soliton for both soliton forms, comparing the highest outlying mode to the adjacent mode energy at 150-Hz with a source depth of 60m. Mode 9 showed the greatest energy difference in decibels. Clearly mode 8 energy values are virtually indistinguishable between both shapes. The obvious difference between mode 9 values shows the sensitivity of shape to the phase at low energy modes. These modes, however can be ignored as their mode energy contributes almost nothing to the entire acoustic pressure field.

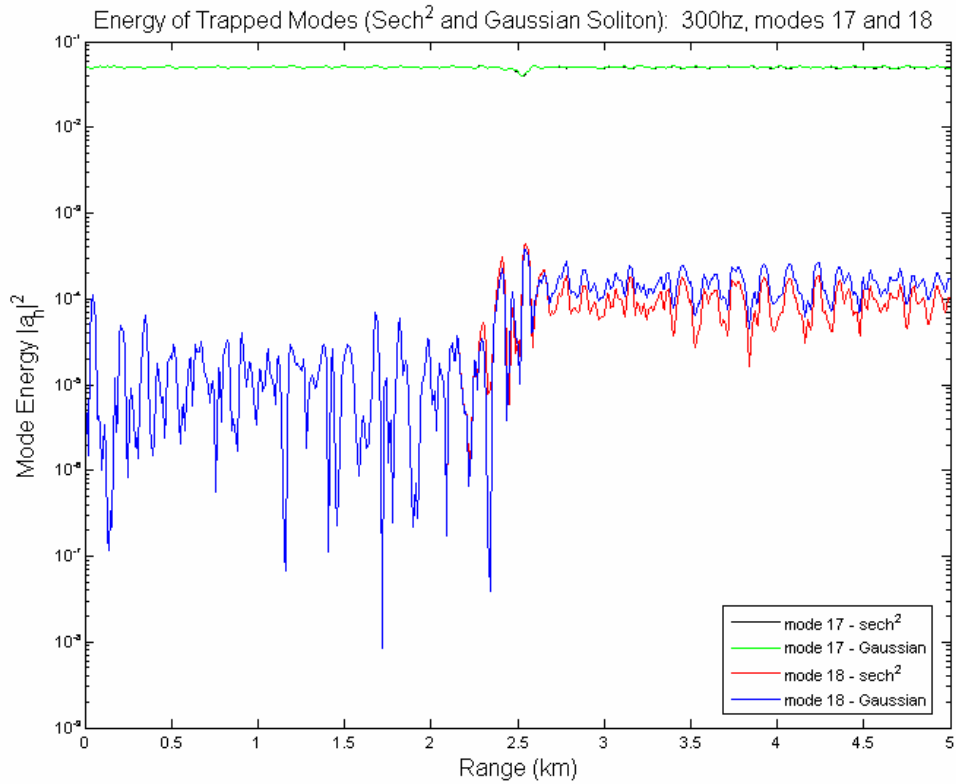


Figure 14. Mode energy $|A_n|^2(r)$ of a single soliton for both soliton forms, comparing the highest outlying mode to the adjacent mode energy at 300-Hz with a source depth of 60m. Mode 18 showed the greatest energy difference in decibels. Clearly mode 17 energy values are virtually indistinguishable between both shapes. The obvious difference between mode 18 values shows the sensitivity of shape to the phase at low energy modes. These modes, however can be ignored as their mode energy contributes almost nothing to the entire acoustic pressure field.

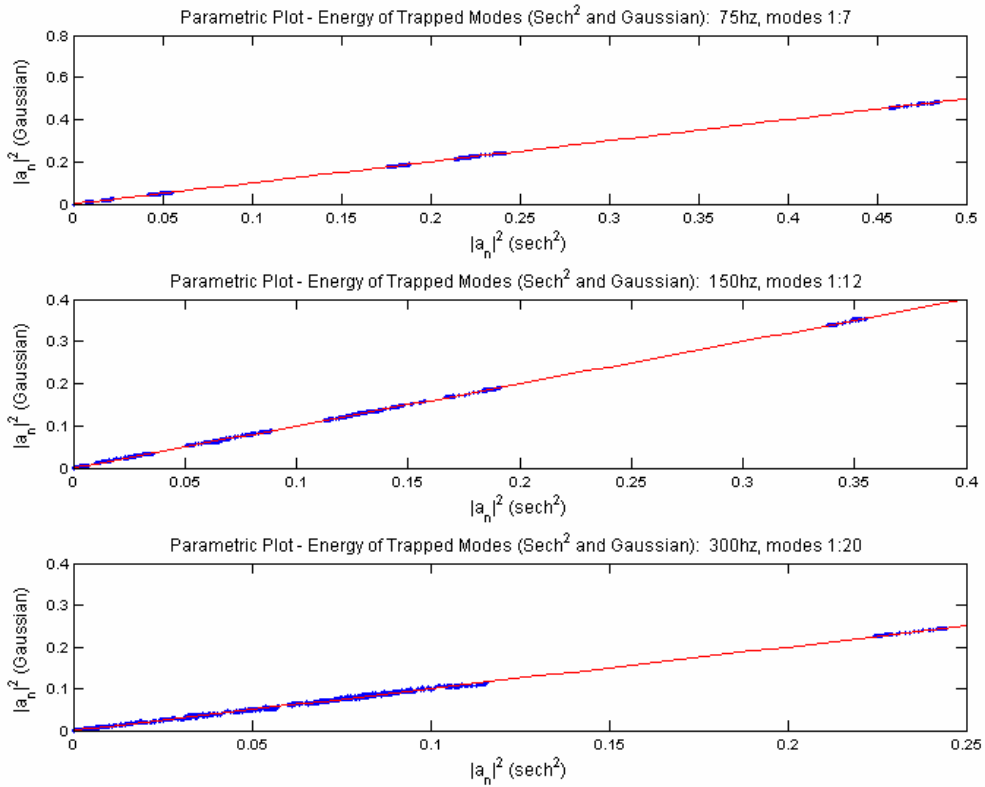


Figure 15. Parametric plot of mode energy for the sech² and Gaussian solitons; for 75, 150 and 300-Hz. The clear linear relationship demonstrates the validity of using a Gaussian shaped soliton in place of the sech² form.

2. Wave Packet

Soliton packets of both sech² and Gaussian forms were incorporated into the model with a comparison made in the same manner as with the single wave. Again a plot of mode energy difference was constructed by averaging the mode energy of the last 1000m for each packet, at each frequency and then forming the relative mode energy $|A_n|^2 / |A_{n0}|^2$ in logarithmic form (Figure 16). Similar results were observed compared to the single wave case. Certain modes demonstrated significant variability but when tested in the same manner as the single wave case, these modes proved to have insignificant energy values and could thus be ignored. Figure 17 shows a comparison between energy values for modes 8 and 9 for 150-Hz; this again demonstrates that variability occurs only with very low energy value modes, which can be ignored. The parametric plot in Figure

18 shows the same linear relationship as the single wave scenario. We thus conclude that the Gaussian form soliton can be used as a very good approximation to the sech^2 form for both single and multi-wave cases.

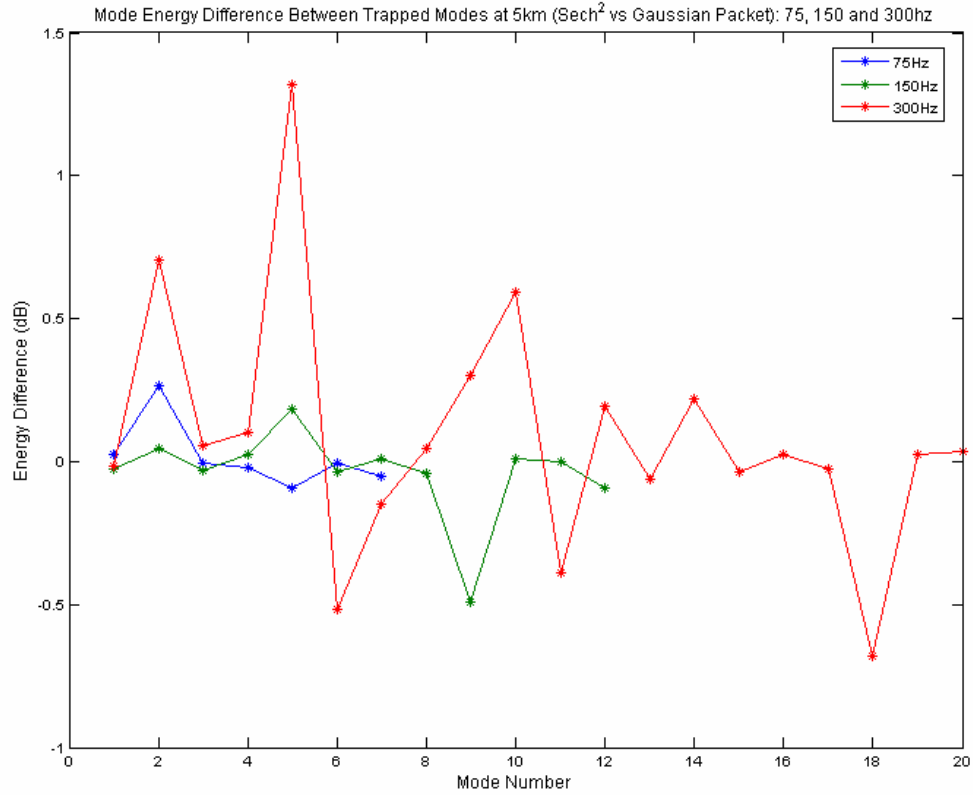


Figure 16. Relative mode energy $10\log_{10}\left(\frac{|A_n|^2}{|A_{n0}|^2}\right)$ between trapped modes for a soliton packet, for all three frequencies, at a range of 5km. The soliton packet is located at 2.5km. These results were obtained from averaging the mode energy of the last 1000m and comparing the difference between the two shapes in logarithmic form.

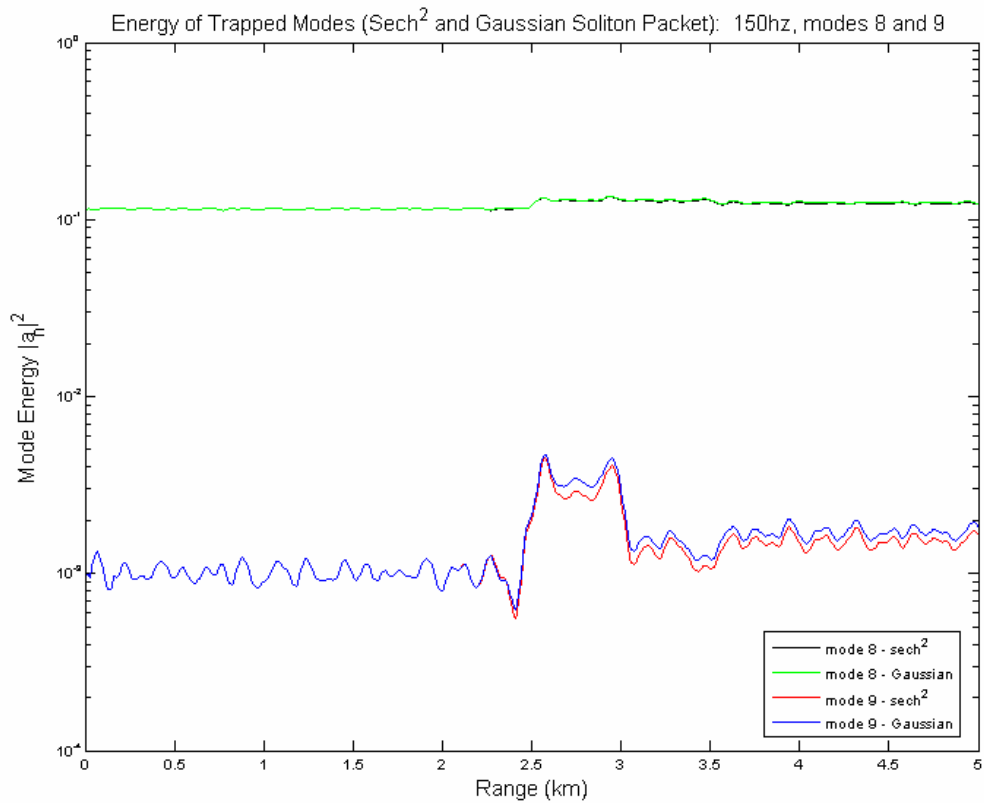


Figure 17. Mode energy $|A_n|^2(r)$ for both forms of a soliton packet, comparing the highest outlying mode to the adjacent mode energy at 150-Hz with a source depth of 60m. Mode 9 shows the greatest energy difference in decibels. Clearly mode 8 energy values are virtually indistinguishable between both shapes. The obvious difference between mode 9 values shows the sensitivity of shape to the phase at low energy modes. These modes, however can be ignored as their mode energy contributes almost nothing to the entire acoustic pressure field. This is a similar result to the single soliton case.

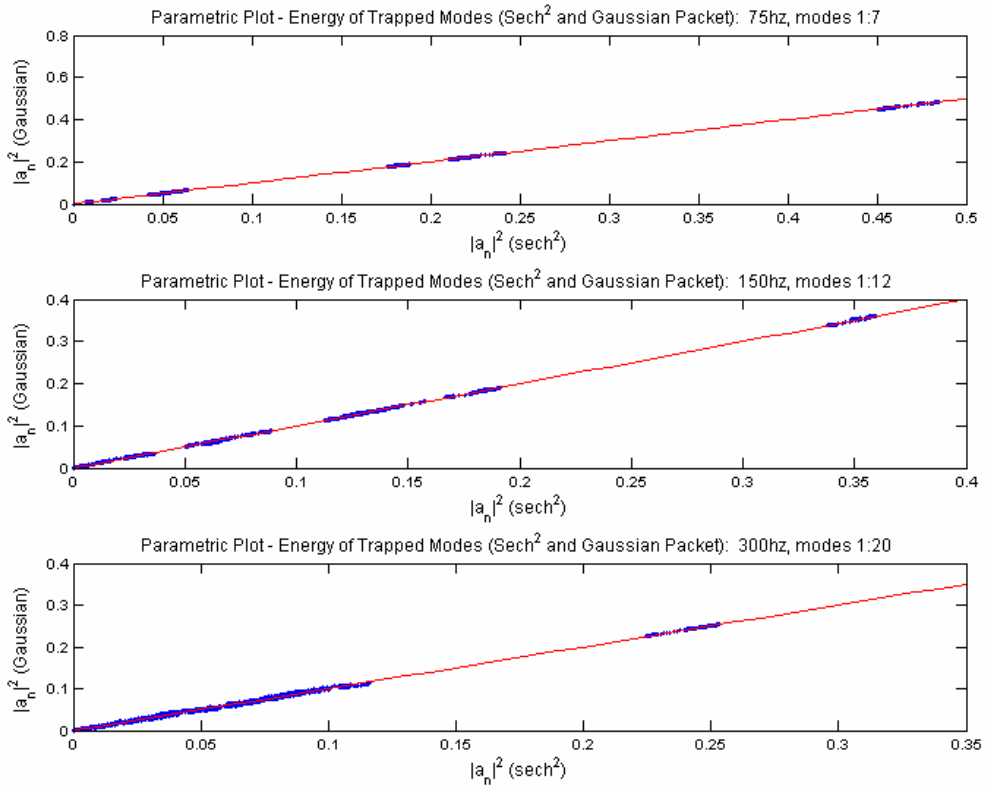


Figure 18. Parametric plot of mode energy for the sech² and Gaussian soliton packets; for 75, 150 and 300-Hz. The clear linear relationship demonstrates the validity of using a Gaussian shaped soliton in place of the sech² form.

B. VARIATION OF SINGLE SOLITON POSITION

1. Numerical Results

The model was run by moving the soliton central range r_0 from 1500 to 3000m; at 5m intervals; for 75, 150 and 300-Hz sound. Again to remove small fluctuations, the average mode energy between 4000 and 5000m was calculated and divided by the initial mode energy to form the relative mode energy. This gave a relative increase or decrease in mode energy as the sound passed through the soliton. Figure 19 shows the amplitude variations for the moving soliton compared to the initial energy of the respective modes at 75-Hz. As the actual energy in mode 2 is very low, the relative change in energy is quite high! To give a better perspective of the other modes, Figure 20 shows the same plot as Figure 19 but with mode 2 removed. Figures 21 and 22 show the 150, and 300-Hz cases respectively. All four plots demonstrate some important issues. Firstly, that there

is no repeating pattern in the mode energies as a function of soliton position. Secondly, at higher frequencies the mode amplitude pattern shows larger deviations as a function of soliton range; and finally, the pattern of energy change is more structured, or shows a higher degree of granularity, at high frequency. Subsequent sections will discuss the theoretical underpinnings of these results.

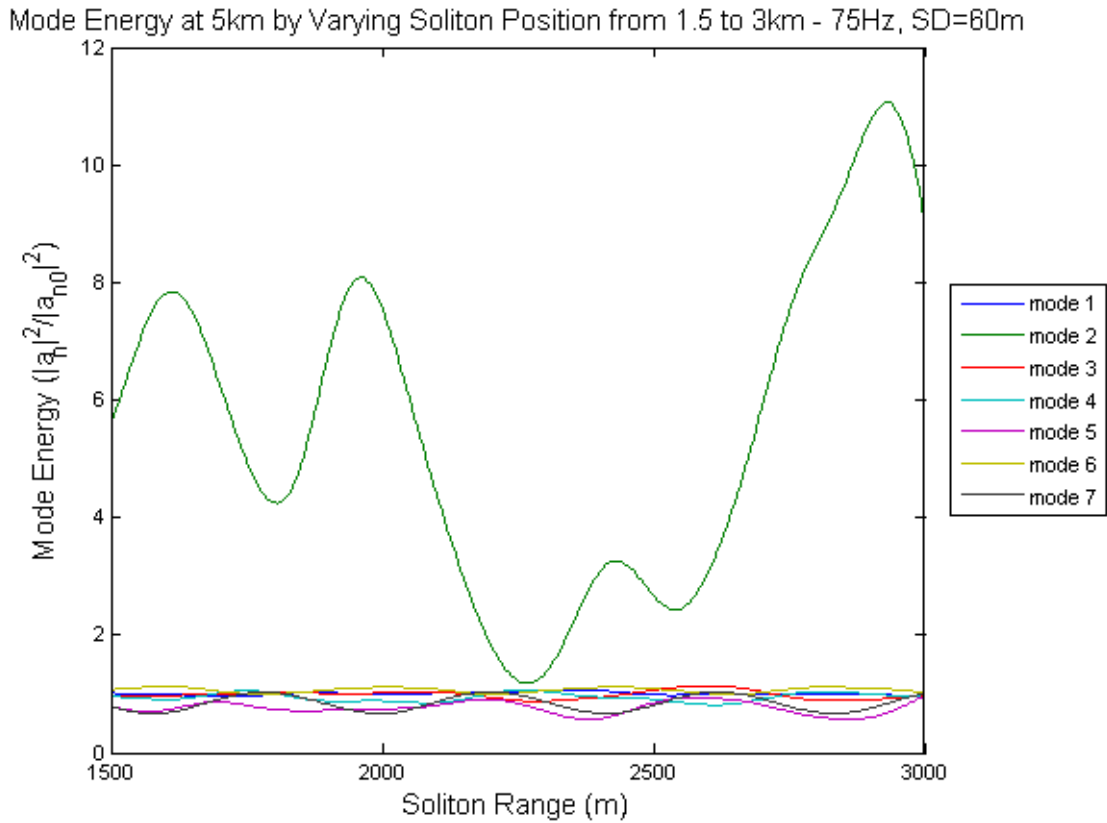


Figure 19. Relative mode energy $|A_n|^2/|A_{n0}|^2$ at 5km (averaged over the last 1000m) for a 75-Hz sound source and a source depth of 60m. This demonstrates a non-repeating mode pattern. Figure 20 shows the same plot with mode 2 removed to give a better perspective of the other modes.

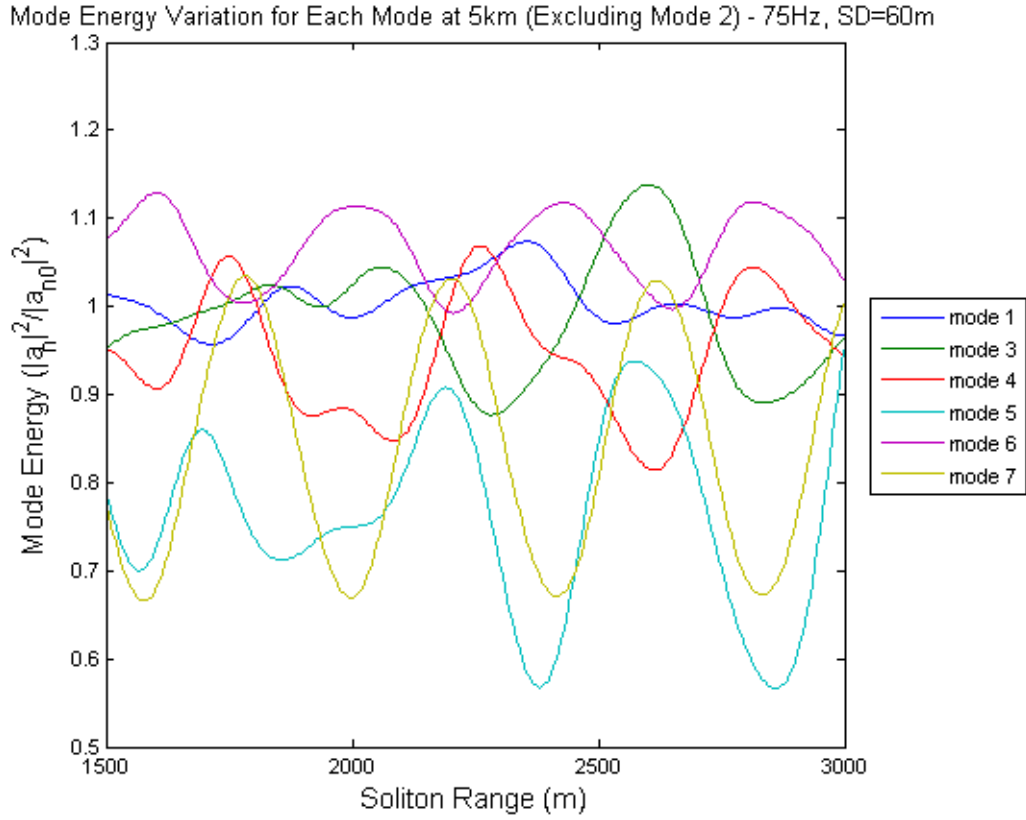


Figure 20. Relative mode energy $|A_n|^2/|A_{n0}|^2$ at 5km (averaged over the last 1000m) for a 75-Hz sound source and a source depth of 60m. This plot excludes mode 2 to give a better perspective of the other modes. Again, this demonstrates a non-repeating mode pattern.

Mode Energy at 5km by Varying Soliton Position from 1.5 to 3km - 150Hz, SD=60m

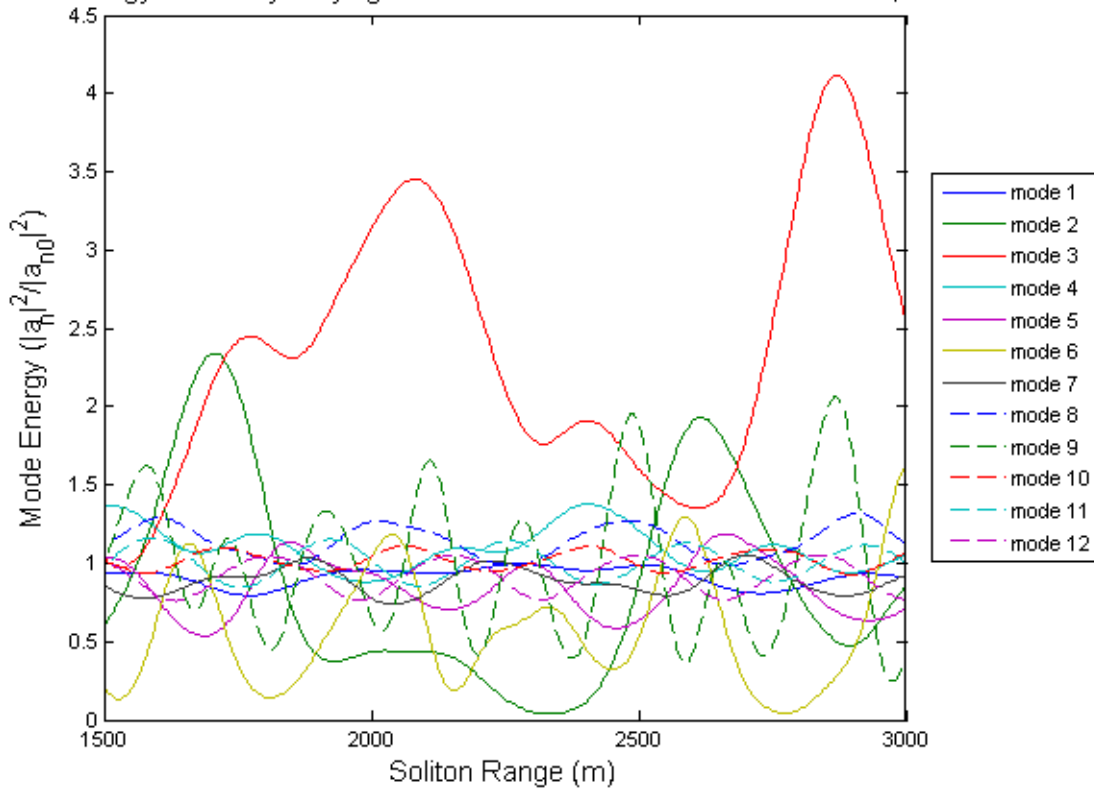


Figure 21. Mode energy $|A_n|^2 / |A_{n0}|^2$ at 5km (averaged over the last 1000m) for a 150-Hz sound source and a source depth of 60m. This demonstrates a non-repeating mode pattern.

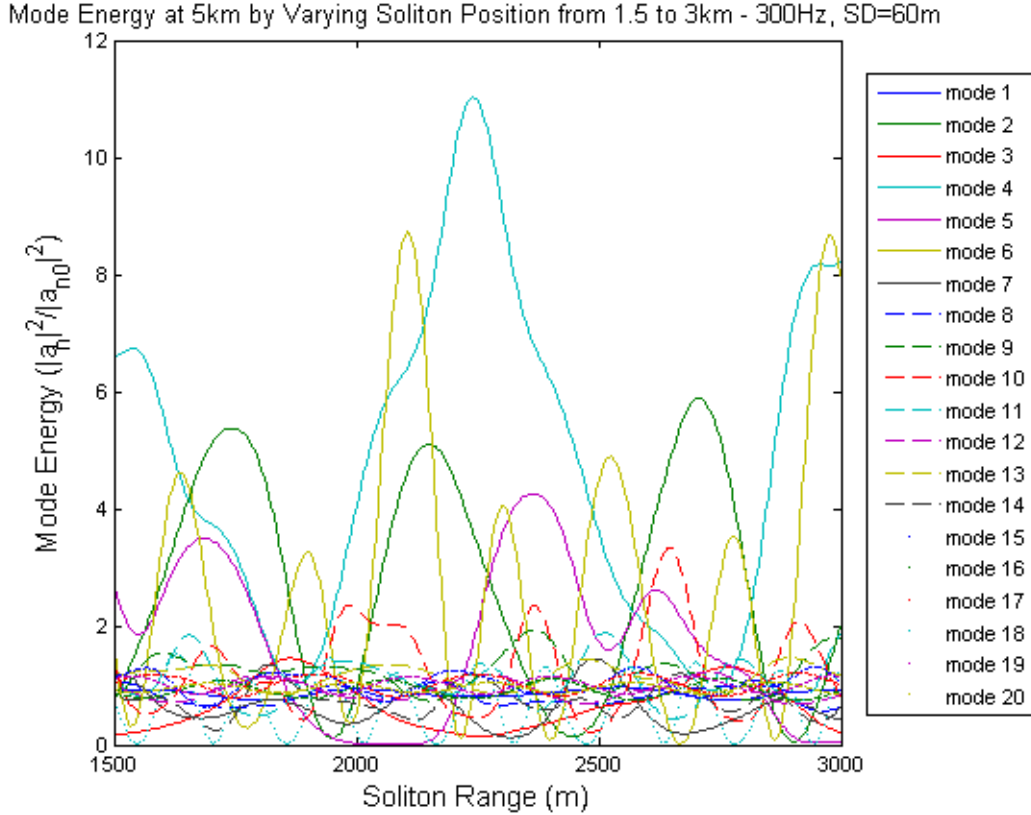


Figure 22. Mode energy $|A_n|^2/|A_{n0}|^2$ at 5km (averaged over the last 1000m) for a 300-Hz sound source and a source depth of 60m. This demonstrates a non-repeating mode pattern.

2. Theoretical Results

The theoretical results were calculated and compared to the simulation discussed in section 1. Figures 23 to 25 show a comparison between simulation and theoretical results (Equation 37) of the seven highest energy modes for the three respective frequencies (naturally all seven trapped modes are represented for 75-Hz). All three cases compare extremely well with the simulation. The mode patterns are virtually identical and there is almost no difference in the mode energy.

The 300-Hz result is very surprising as it was expected that at higher frequencies, higher order theory would have been required to resolve both the mode pattern and the mode energy variations, to some degree of accuracy. This result, though surprising, is very promising. Higher frequencies will need to be tested in future research to determine the limit of the first order theory.

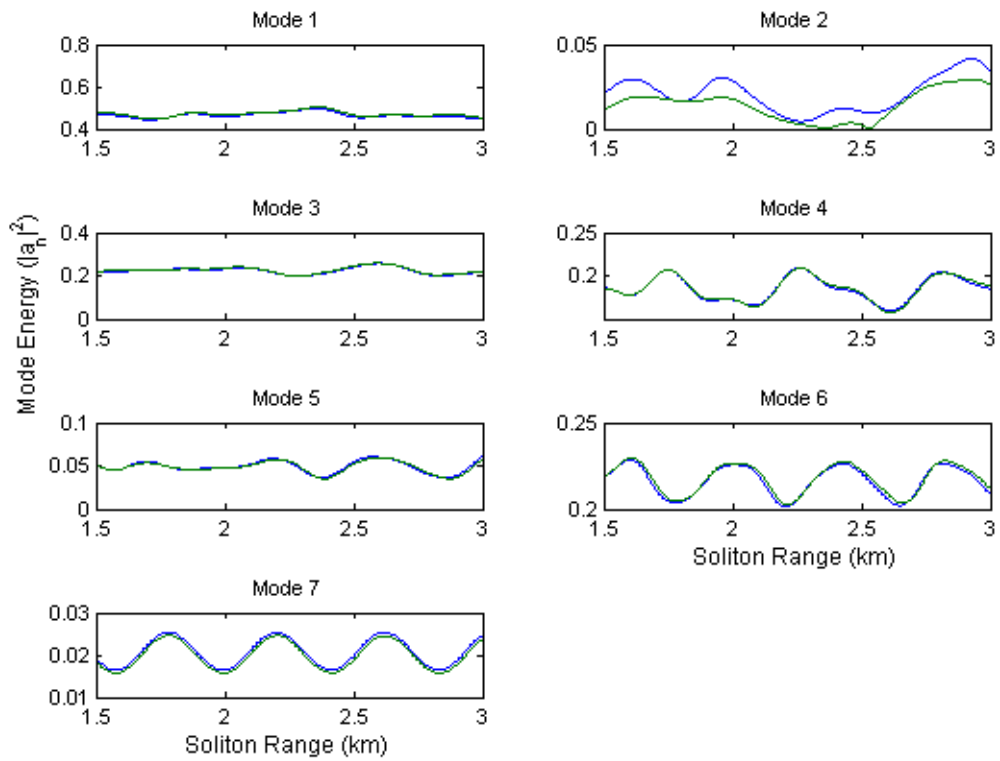


Figure 23. Comparison of simulated (blue) and theoretical (green) results for a 75-Hz sound source at 60m, and a single wave moving between 1.5 and 3km. There is clearly very good agreement between the two results with almost identical mode pattern and virtually the same mode shape.

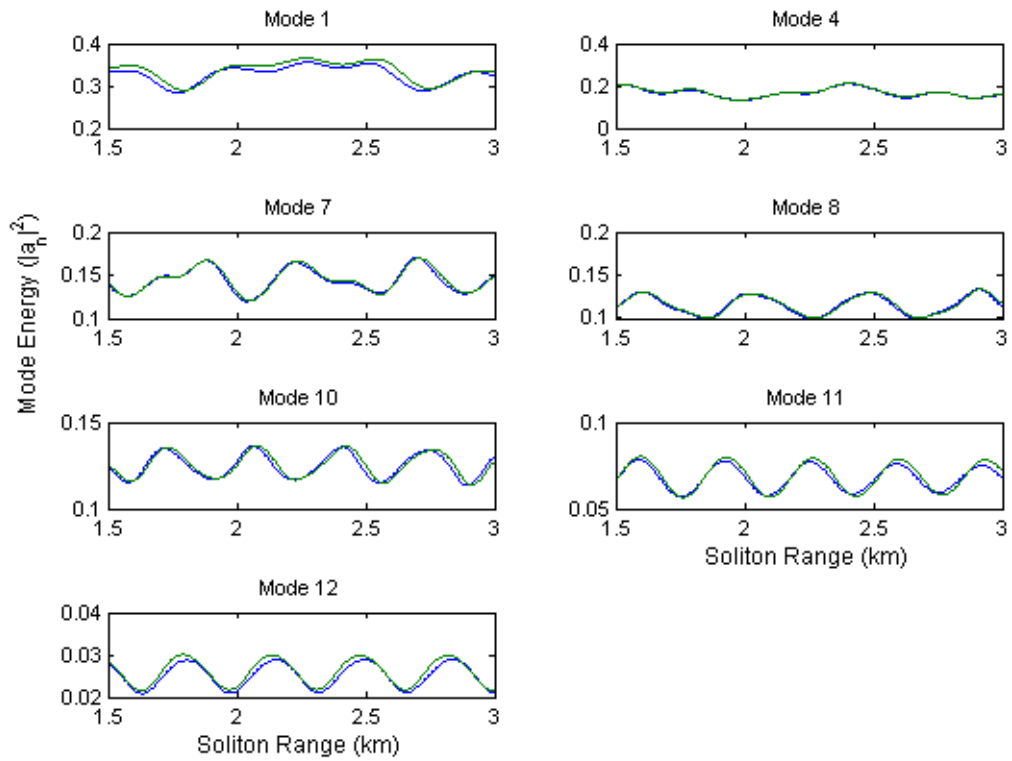


Figure 24. Comparison of simulated (blue) and theoretical (green) results for the seven highest energy modes of a 150-Hz sound source at 60m, and a single wave moving between 1.5 and 3km. There is clearly very good agreement between the two results.

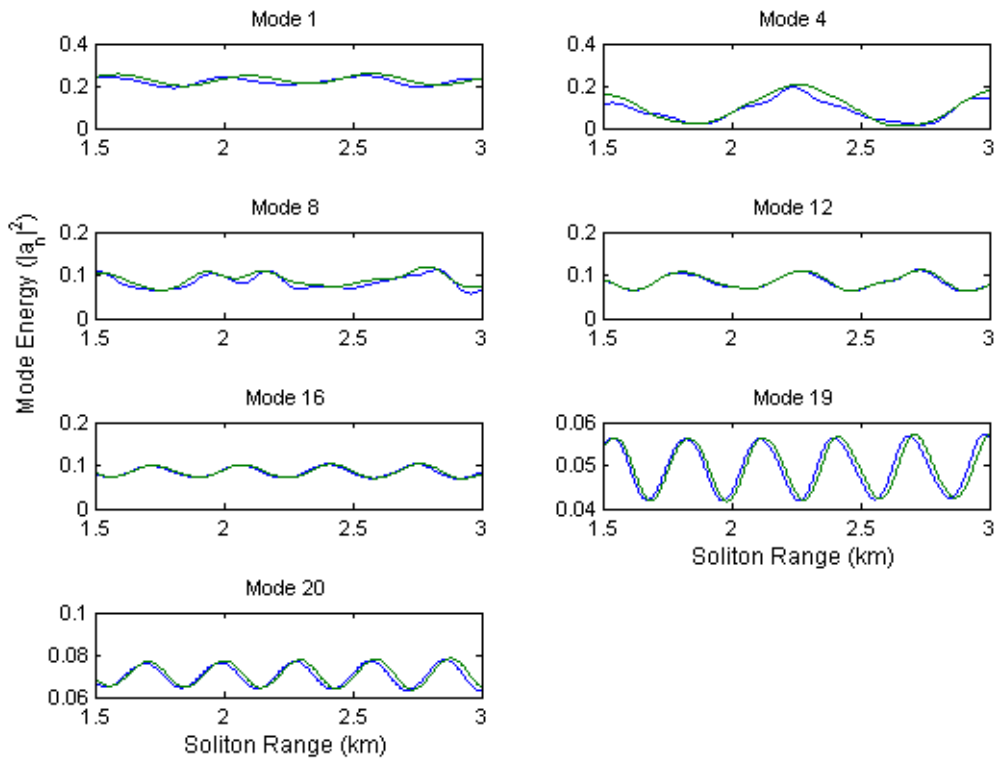


Figure 25. Comparison of simulated (blue) and theoretical (green) results for the seven highest energy modes of a 300-Hz sound source at 60m, and a single wave moving between 1.5 and 3km. The similarity in both the mode pattern and mode energy is surprising at this relatively high frequency.

Figure 26 shows a parametric plot of actual (simulated) versus theoretical mode energies for all three frequencies for all trapped modes. Figure 27 shows the same plot but only for the 7 highest modes for 150 and 300-Hz. These plots demonstrate a number of important aspects. Firstly, the disorganization in the plot is an indication of mode pattern similarity; the less disorganized the plot, the closer the pattern of the theory matches the simulation. There is a clear linear relationship between the theory and the actual results which becomes progressively more disorganized with higher frequency; however, the strength of the linear relationship at 300-Hz was unexpected. Secondly, the slope of the line relative to the slope of one, gives a comparison of energy values between the theory and the simulation. If the plot sits below the line, the theory under predicts energy values and if above the line the theory over predicts. For all three cases the theory

predicts the mode energy values to a high degree of accuracy though there is a very slight tendency toward over prediction at 300-Hz. Finally, a comparison between Figures 26 and 27 shows that there are areas which demonstrate significantly more disorganization with lower energy modes; for example, 150-Hz with $|a_n|^2$ values between 0.05 and 0.08. This is not to say that all low energy modes are irresolvable with the first order theory. Figure 26 shows a clear linear relationship for both 150 and 300-Hz for many low energy modes. The reason as to why some low energy modes are more affected than others is possibly due to the inability of the theory to deal with mode coupling from a high energy mode to a low energy mode or vice versa. It is expected that modes which couple from a relatively low energy mode to another low energy mode maintain good agreement between theory and simulation results.

The results for all three frequencies demonstrate that the acoustic pressure field can be predicted in the presence of a soliton environment. It is expected that many of the discrepancies between the theoretical and the actual results, for low energy modes, will be resolved with higher order theory.

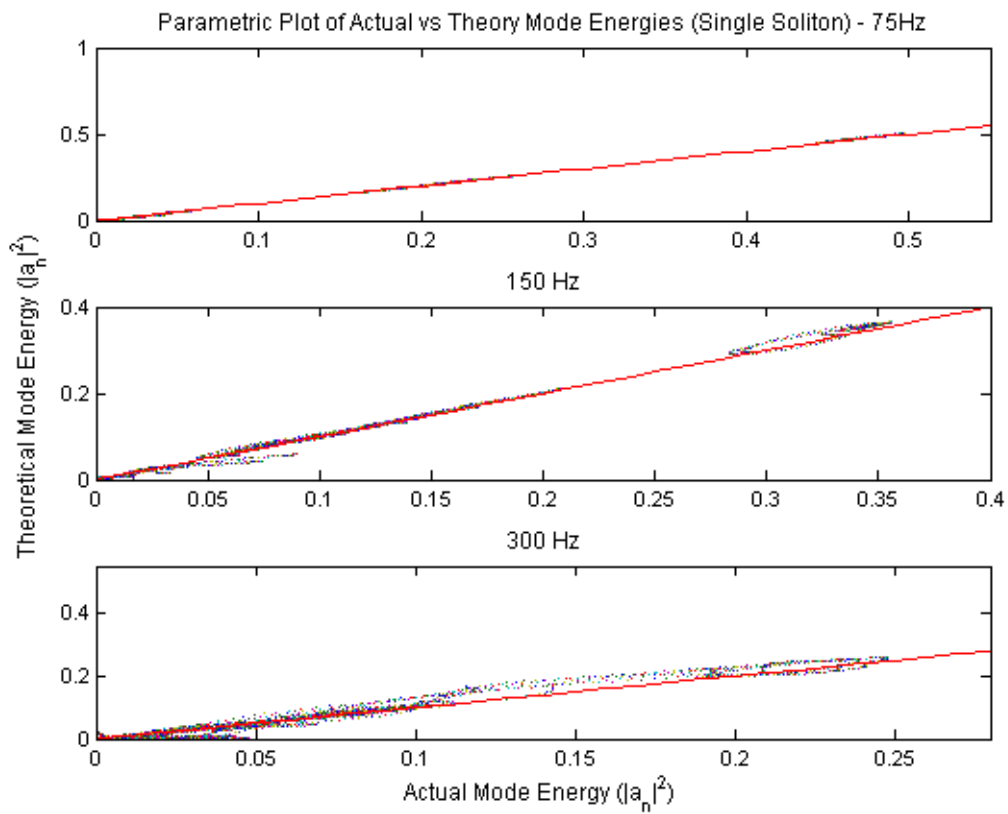


Figure 26. Parametric plot of simulated versus theoretical mode energies (for all modes) for a single soliton with a 60m source depth. The red line shows a linear relationship.

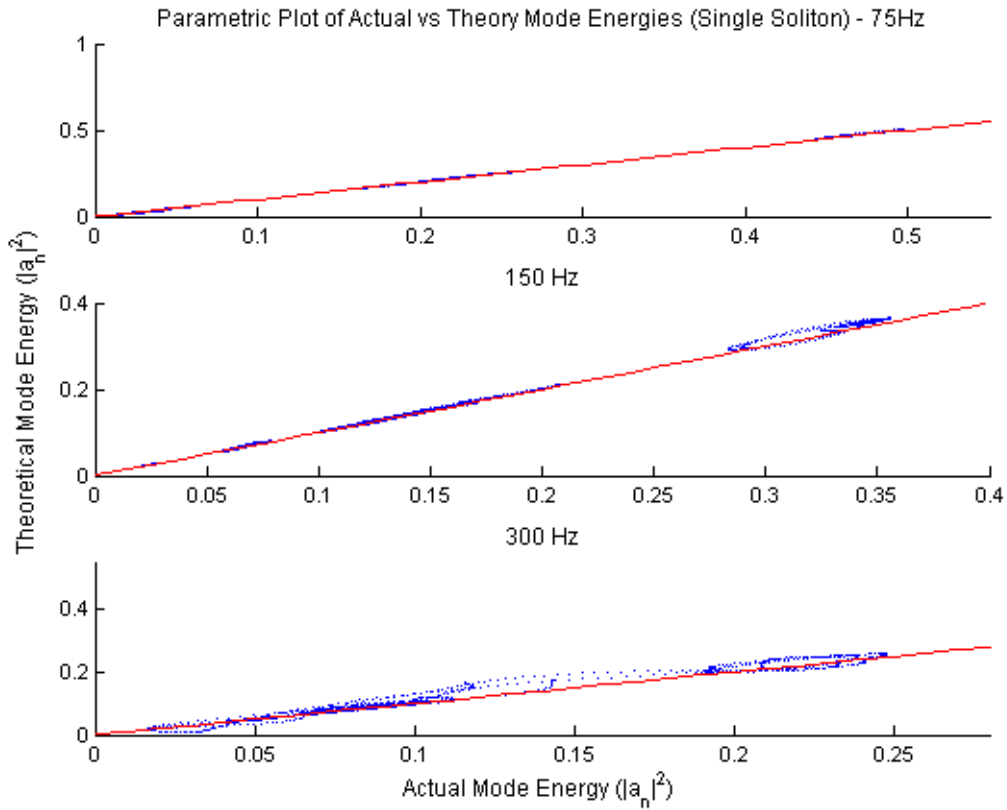


Figure 27. Parametric plot of simulated versus theoretical mode energies (for the seven highest energy modes) for a single soliton with a 60m source depth.

The strong agreement between the theory and the simulated results makes the theory useful in interpreting the simulations from section 1. First we address the issue of the non-periodic structure of $|A_n|^2(r_0)$. From the theory (Equation 37) the parameter r_0 appears as $\sin(l_{mn}r_0)$. Thus the pattern $|A_n|^2(r_0)$ is controlled by the beat frequency l_{mn} . A plot of mode number versus horizontal wave number l_n is shown in Figure 28. The Figure shows a non linear relationship between horizontal wave number and mode number for all frequencies. This means that the wavenumbers are not commensurate, thus the $\sin(l_{mn}r_0)$ term will not give a repeating pattern when summed in Equation (37). This explains the non-periodic structure of $|A_n|^2(r_0)$ observed in the simulation.

Next we address the issue that the mode energy fluctuations seem to grow with frequency. Figures 19 to 22 revealed that the strength of mode coupling increased with

increasing frequency. Terms *III*, *IV* (C_{mn}) and *VI* (which we will call D_{mn}) of the modal evolution Equation (36) all contribute to the strength of mode coupling. Figure 29 shows a plot of terms *IV* and *VI* as well as the combination to the two. There is a clear linear increase in C_{mn} values with increasing frequency (primarily due to the k_0 term) while D_{mn} remains relatively unchanged with frequency in spite of the fact that l_{mn} can have smaller values at high frequency. The net result is that the coupling terms (predominately C_{mn}) always increase the coupling strength. Figures 19 to 22 however, show that coupling strength does not increase for all modes with frequency. Figure 30 is a plot of the log of the initial amplitude values, or the excitation energy which appears in Equation (38) as $A_m(0)A_n(0)/|A_n(0)|^2$ (which we will call ψ_{mn}); and demonstrates that the complexity of this excitation energy has a strong effect on the coupling magnitude. This term can either magnify or diminish the coupling strength with frequency, caused by the other coupling terms; thus the coupling magnitude does not necessarily increase for all modes with increasing frequency.

Finally we address the issue of the increased structure of the pattern $|A_n|^2(r_0)$ for higher frequencies. The sensitivity of $|A_n|^2(r_0)$ is naturally dependent on the $\sin(l_{mn}r_0)$ term of the modal power Equation (37) as this is the only term dependent on the soliton location. Thus the structure of the pattern $|A_n|^2(r_0)$ depends on the beat wavenumbers l_{mn} ; if l_{mn} is small this contributes to slow variation with r_0 while for l_{mn} large, this contributes to rapid variations with r_0 . Figure 31 shows a plot of allowable difference wave number verses frequency. There is an obvious increase in the l_{mn} values with frequency, thus the increase in granularity with increasing frequency, observed in Figures 19 to 22, is explained.

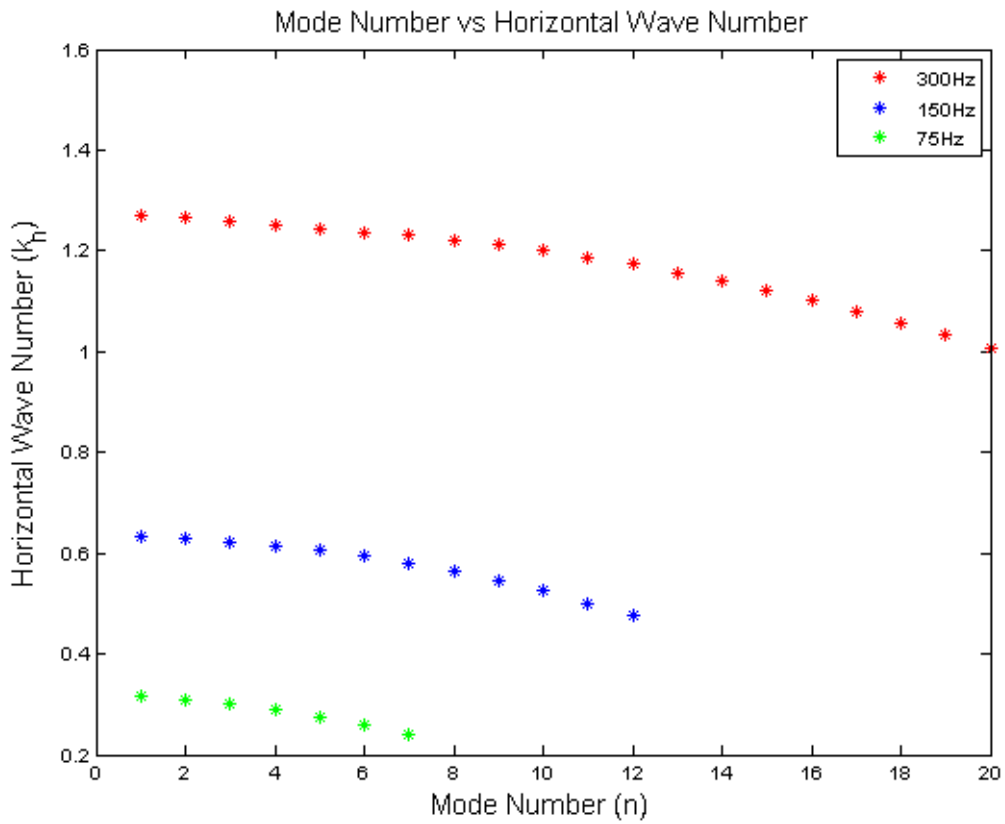


Figure 28. Horizontal wavenumber versus node number, for all three frequencies, computed by the solution of the unperturbed mode equation (Equation 6).

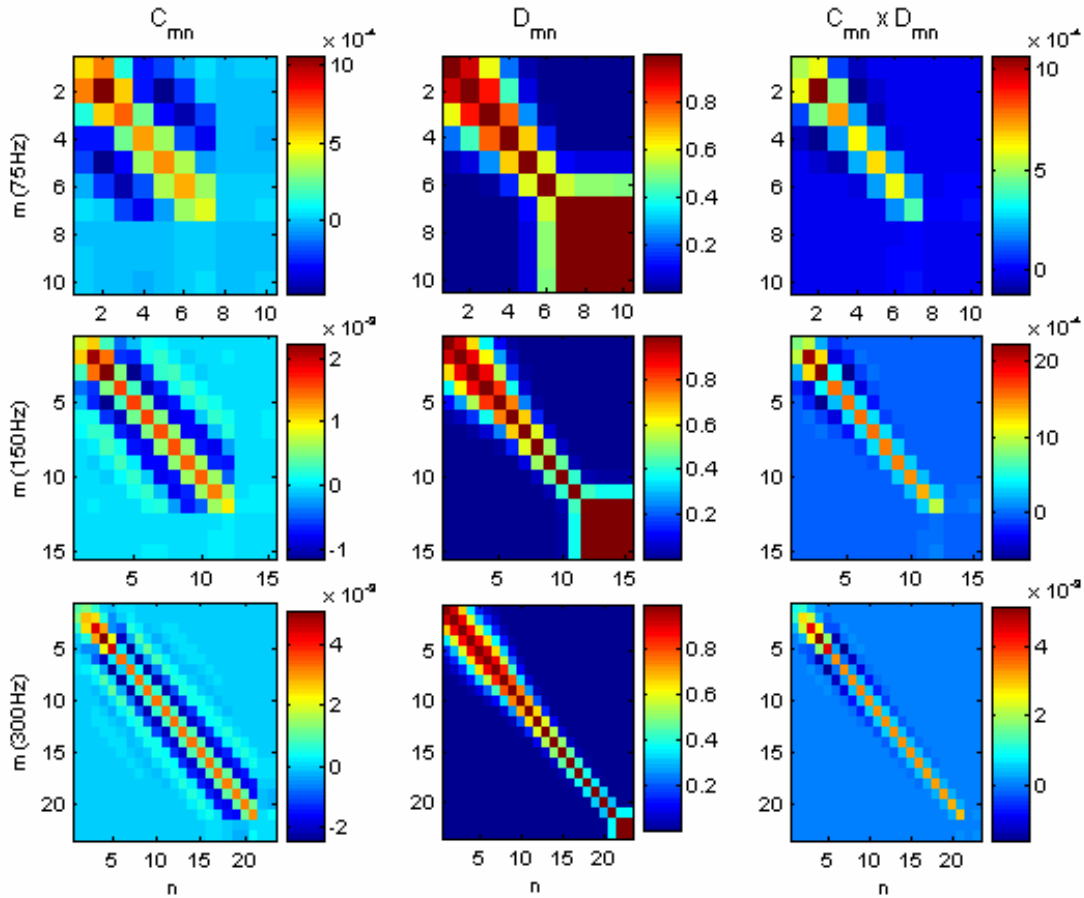


Figure 29. Terms IV and VI of the modal evolution Equation (36). There is a clear linear increase of C_{mn} with frequency while D_{mn} shows very little variation with frequency. Together, these terms always act to increase the coupling strength with increasing frequency.

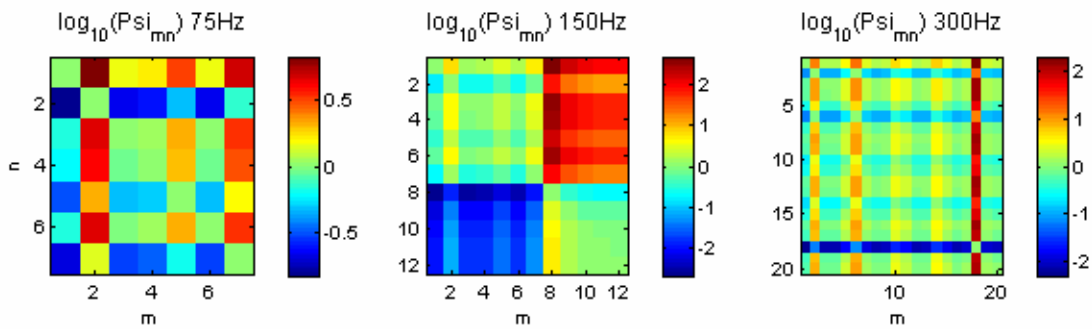


Figure 30. The complex nature of the excitation energy shows that it can magnify or diminish the increase in mode coupling strength with frequency, caused by the terms C_{mn} and D_{mn} .

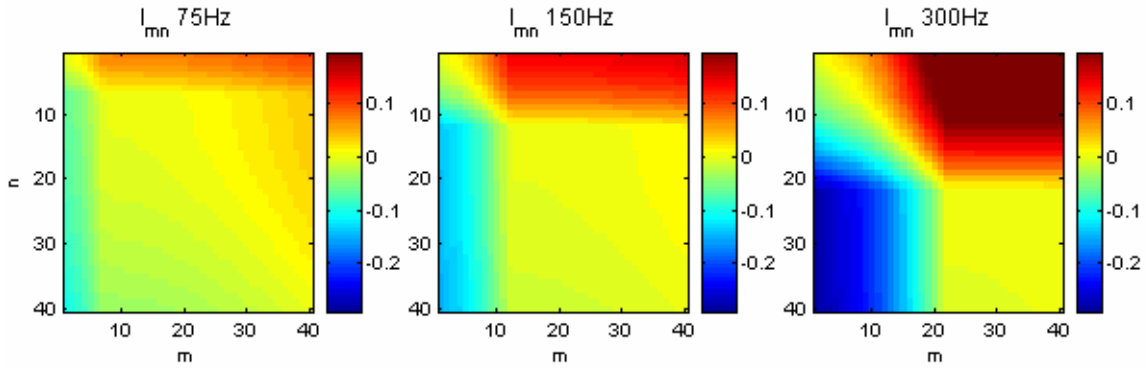


Figure 31. Allowable difference wavenumbers as a function of increasing frequency. The clear increase in allowable l_{mn} values with increasing frequency explains the increased granularity (or structure) observed with increasing frequency in Figures 19 to 22.

C. VARIATION OF POSITION WITH A SOLITON WAVE PACKET

1. Numerical Results

The model was run again with a source depth of 60m for all three frequencies, but with a wave packet in place of the single soliton. The results were very similar to the previously discussed single soliton case where we observed a non repeating beat pattern; larger deviations in mode amplitude pattern as a function of range; and a higher degree of granularity at higher frequencies. Figure 32 shows the amplitude variations for the moving packet compared to the initial energy of the respective modes at 150-Hz.

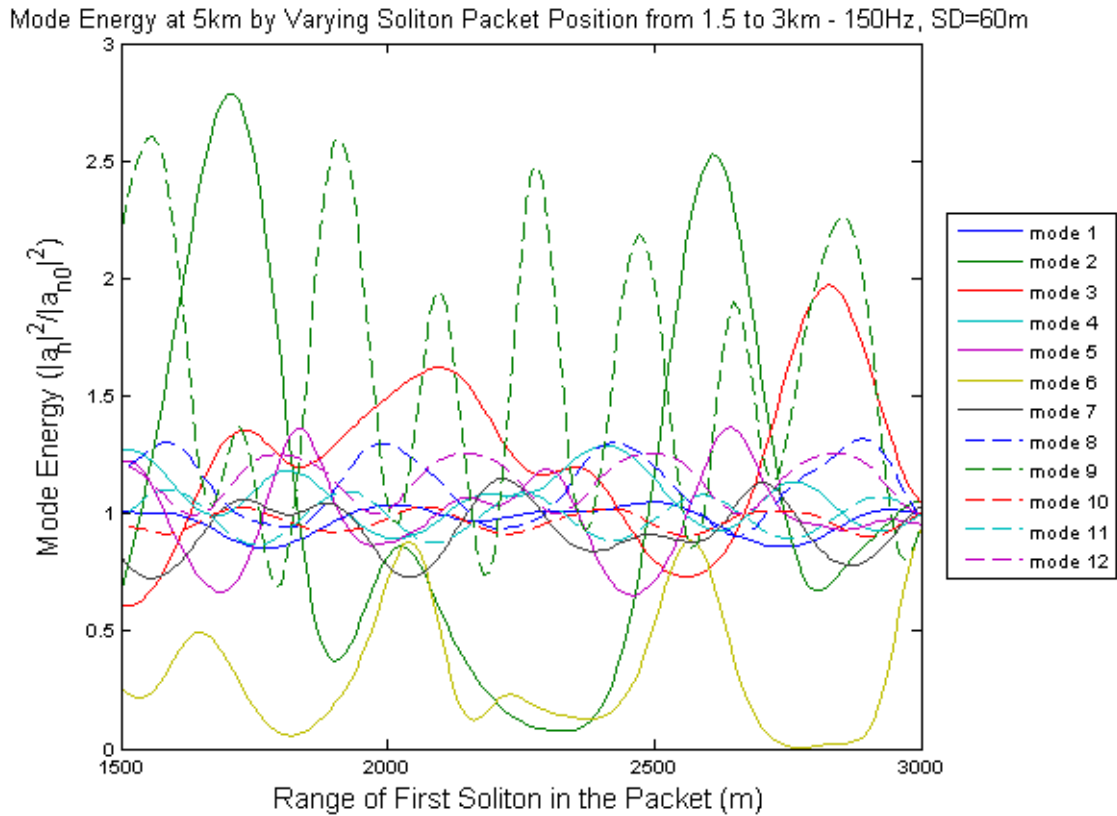


Figure 32. Mode energy $|A_n|^2/|A_{n0}|^2$ at 5km (averaged over the last 1000m) for a wave packet with a 150-Hz sound source and a source depth of 60m. This demonstrates a non-repeating mode pattern.

2. Theoretical Results

Figure 33 shows the comparison between the theory and the simulation for a wave packet moving between 1.5 and 3km, with a source depth of 60m and a frequency of 150-Hz. For the sake of continuity the same modes are used as in the single wave case (mode 12 would be replaced by mode 5 in the wave packet case if the highest seven energy modes were used). The results for all three frequencies again show excellent agreement between the theory and the simulation. The similarity in mode pattern to the single wave case leads to the assumption that the first soliton in the packet has the greatest impact on mode energy variations at these frequencies. Even the 300-Hz case (Figure 34) shows that the first wave in the packet is the most important; however, higher frequencies are expected to show more sensitivity to additional waves.

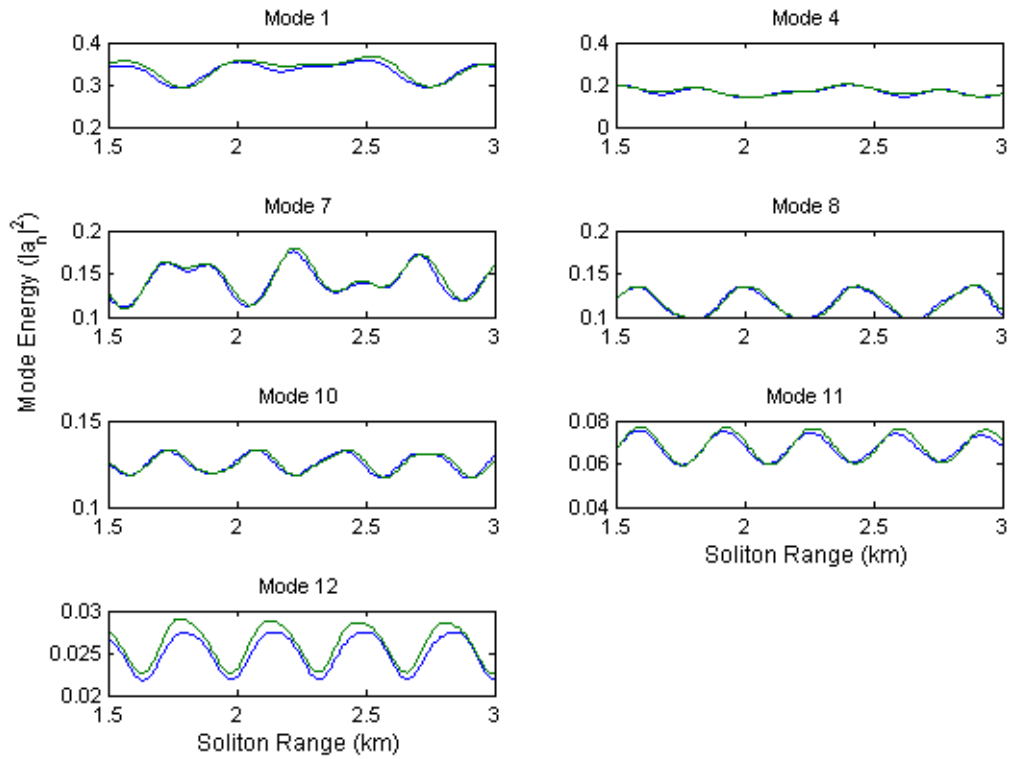


Figure 33. Comparison of simulated (blue) and theoretical (green) results for a 150-Hz sound source at 60m, and a wave packet moving between 1.5 and 3km (the same modes are compared as in the single wave case). There is clearly very good agreement between the two results; and the similarity in the pattern to the single wave case indicates that the first soliton is the most important in determining mode coupling at this frequency.

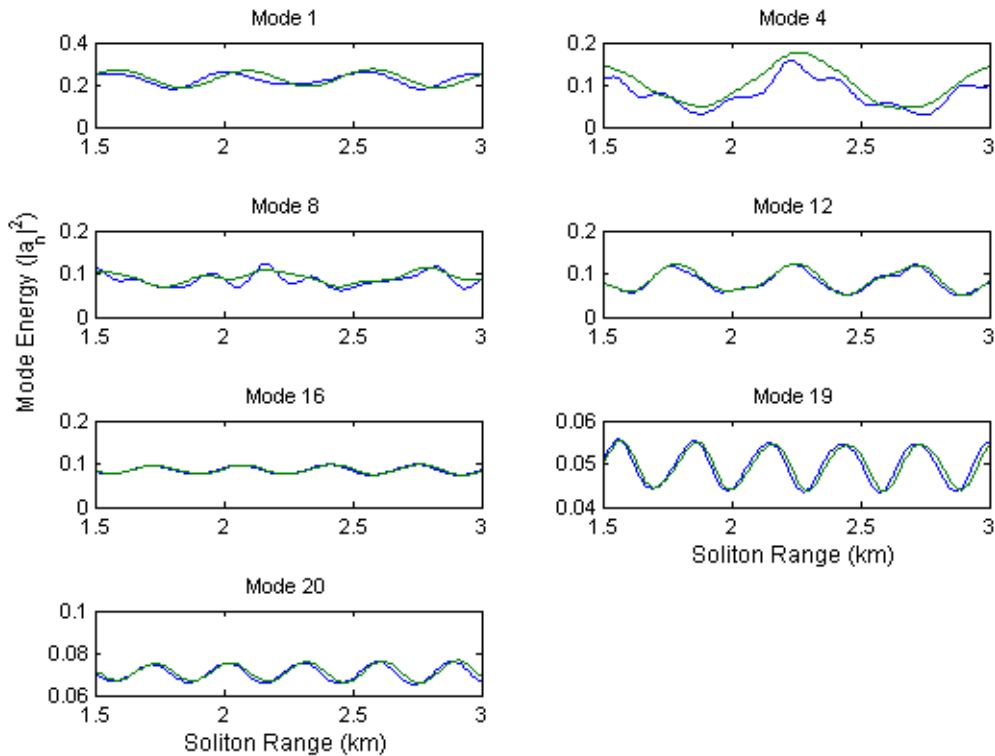


Figure 34. Comparison of simulated (blue) and theoretical (green) results for a 300-Hz sound source at 60m, and a wave packet moving between 1.5 and 3km (the same modes are compared as in the single wave case). Again, the agreement between the two results in both the mode pattern and the mode energy is very good. The lack of variation in the wave pattern between the single wave case indicates that even at this frequency, the first wave in the packet dominates the coupling regime.

Figures 35 and 36 show the parametric plots of actual versus theoretical mode energies, for the wave packet case. The results confirm the ability to predict the acoustic pressure field in the presence of a wave packet, for the frequencies trialed. Future research should test the higher frequencies than those examined here, to determine when, if ever, the pattern becomes sensitive to multiple solitons. Again, it is expected that the discrepancies between the theoretical and actual mode energies, for higher frequencies and lower energy modes will be resolved with higher order theory.

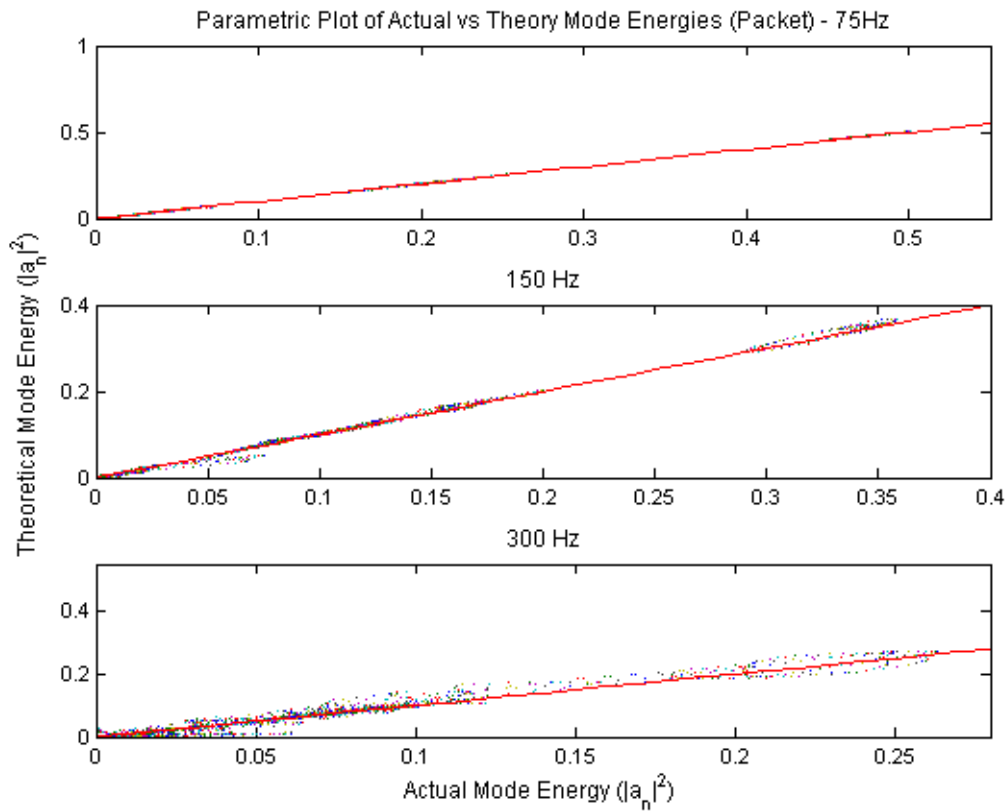


Figure 35. Parametric plot of actual (simulated) versus theoretical mode energies (for all modes) for a wave packet with a 60m source depth.

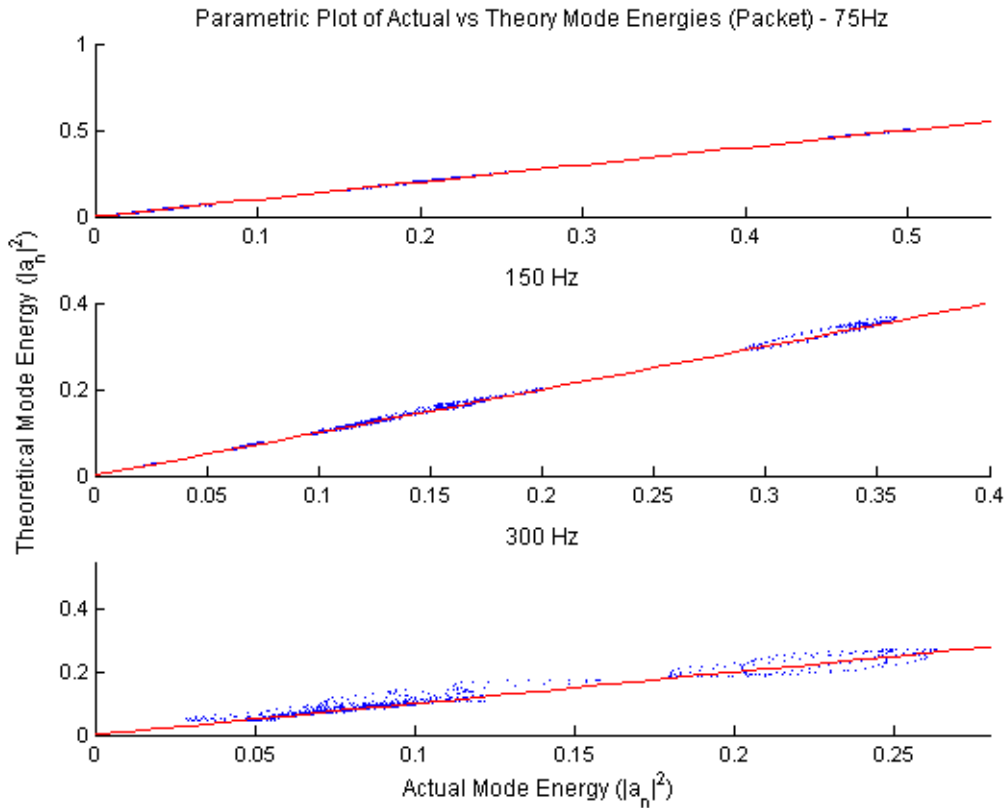


Figure 36. Parametric plot of actual (simulated) versus theoretical mode energies (for the seven modes compared in the single soliton case) for a wave packet with a 60m source depth.

D. VARIATIONS IN SOURCE DEPTH

1. Single Soliton

Figure 37 shows the comparison between the theory and the simulation for a wave packet moving between 1.5 and 3km, with a source depth of 10m and a frequency of 150-Hz, for the seven highest energy modes. There is clearly good agreement between the theory and the actual results in both the mode pattern and the mode energy values. In fact, the parametric plots (Figures 38 and 39) shows a better agreement in both pattern and energy values for 150 and 300-Hz, compared to a source depth of 60m. The same relationships seen in the 60m case are apparent in the shallow water case. An increase in frequency leads to a slightly greater disagreement in mode pattern and energy values when comparing the theory and the actual results. The conclusion is made that the theory is valid for predicting the acoustic pressure field in a single soliton environment for both a deep and a shallow source depth.

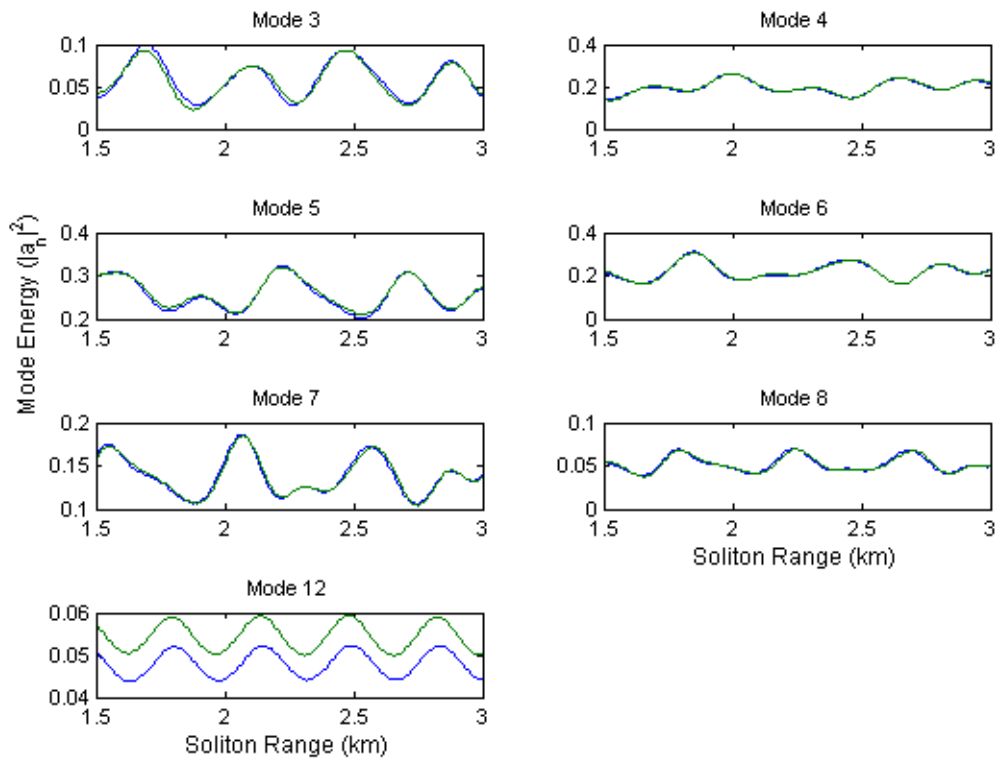


Figure 37. Comparison of simulated (blue) and theoretical (green) results for the seven highest energy modes of a 150-Hz sound source at 10m, and a single wave moving between 1.5 and 3km. There is clearly very good agreement between the two results.

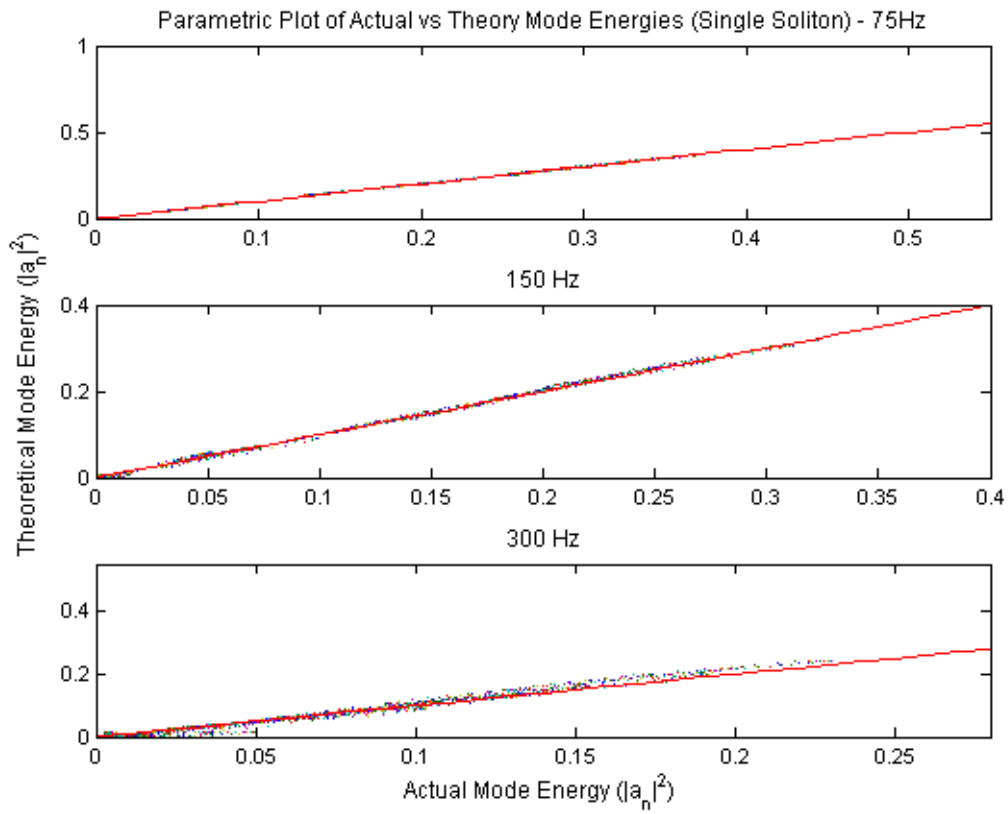


Figure 38. Parametric plot of actual (simulated) versus theoretical mode energies (for all modes) for a single soliton with a 10m source depth.

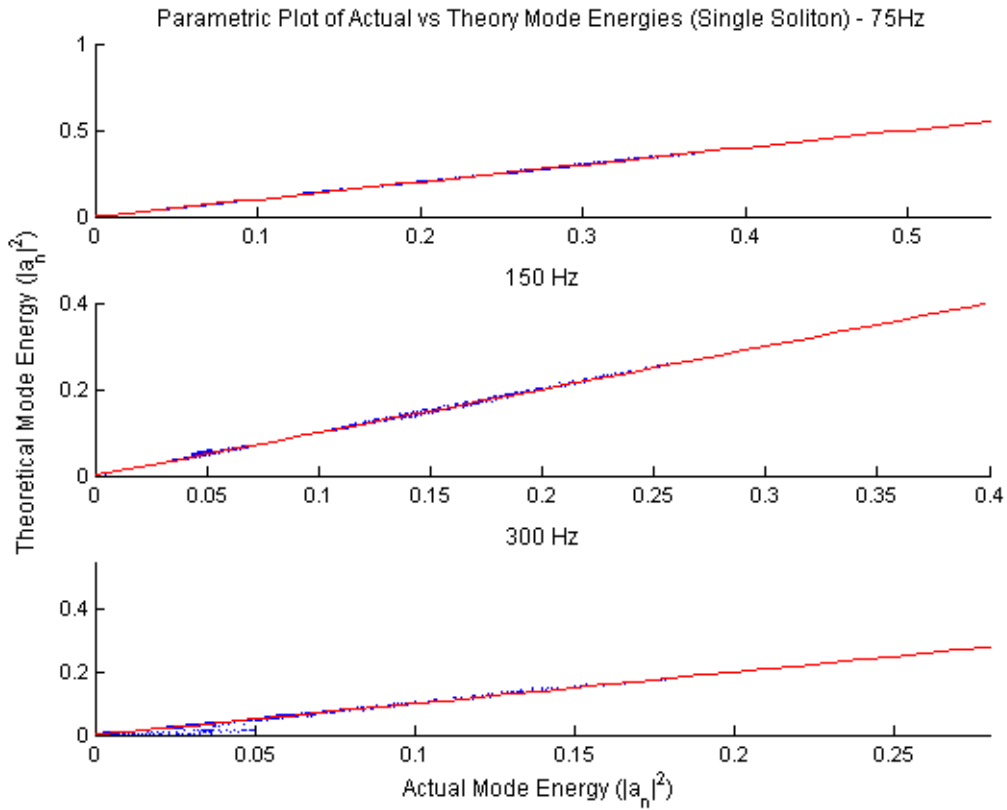


Figure 39. Parametric plot of actual (simulated) versus theoretical mode energies (for the seven highest energy modes) for a single soliton with a 10m source depth.

2. Wave Packet

As with the single soliton case, with a source depth of 10m, the wave packet case shows better agreement between the theory and the actual results compared with the deep source of 60m. Parametric plots at Figures 40 and 41 again show the same relationships in discrepancies between theoretical and actual results, previously observed. Once again the conclusion is reached that the theory can predict the acoustic pressure field in a multi-wave environment for both a deep and shallow source depth.

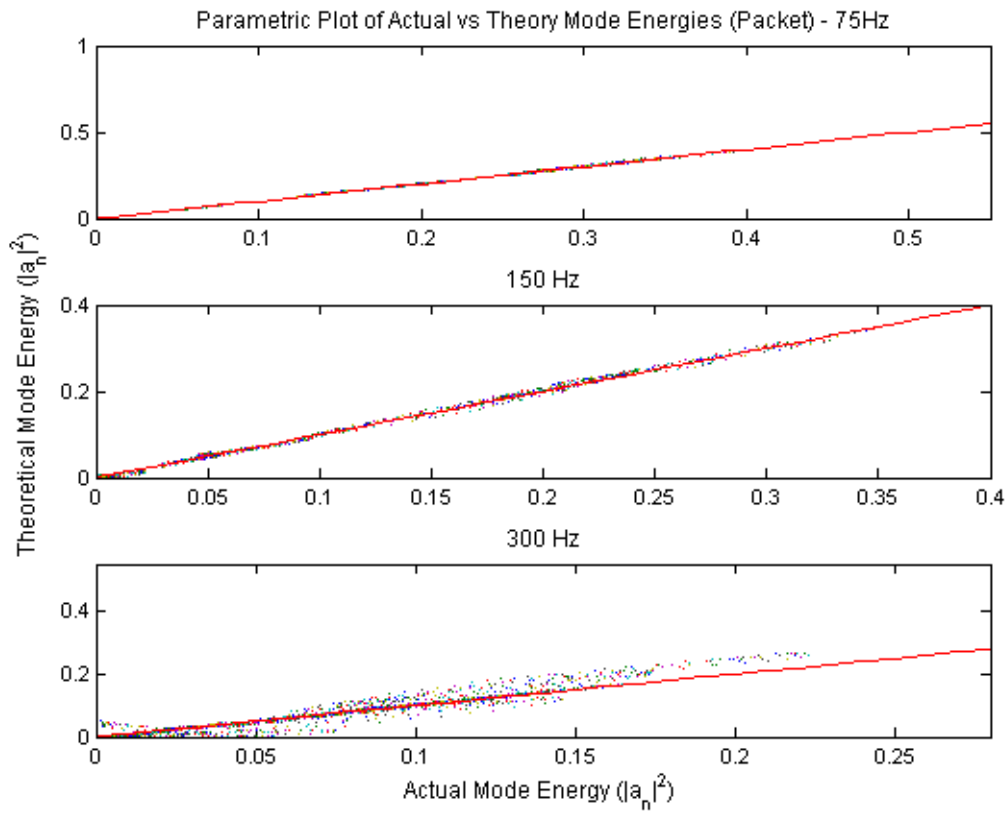


Figure 40. Parametric plot of actual (simulated) versus theoretical mode energies (for all modes) for a wave packet with a 10m source depth.

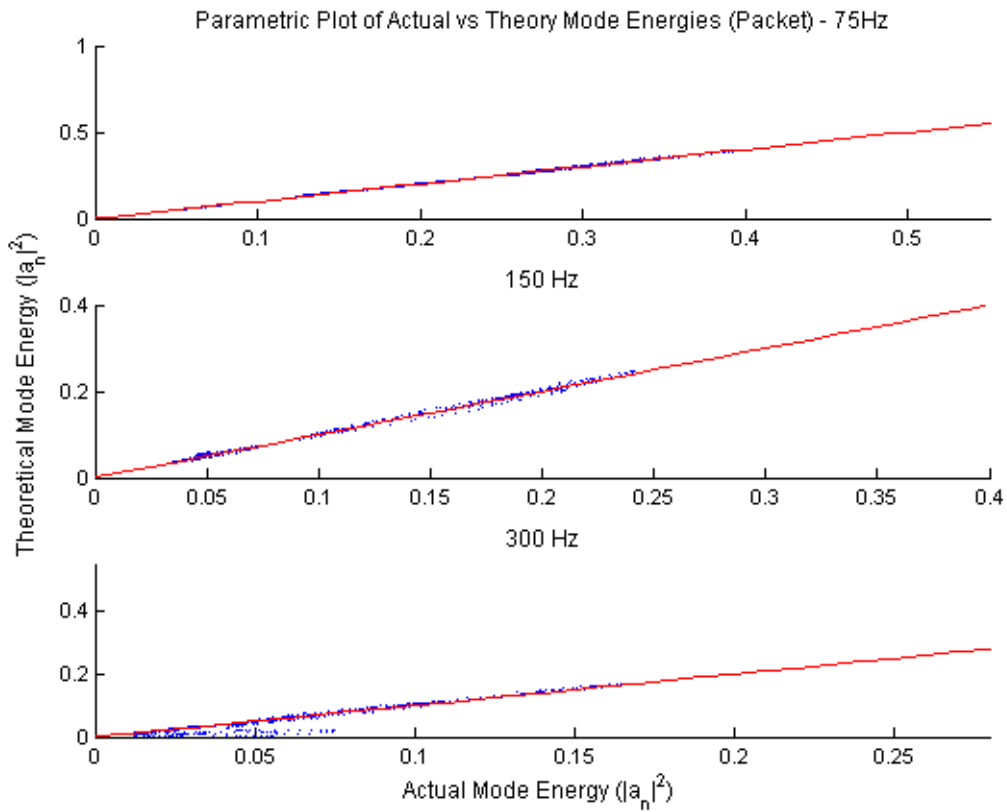


Figure 41. Parametric plot of actual (simulated) versus theoretical mode energies (for the seven modes compared in the single soliton case) for a wave packet with a 10m source depth.

IV. CONCLUSION

A 2D parabolic wave simulation was developed to model acoustic propagation and mode coupling through internal solitary waves; and to test against a weak scattering theory (developed by Colosi), whose primary physics is a Bragg scattering mechanism.

Historically a sech^2 form has been used to model internal solitary waves as it is a solution to the KDV wave equation. A Gaussian form is very similar to the sech^2 form but is mathematically more expedient when looking at weak scattering theory. To see if the Gaussian form could replace the sech^2 , the two forms were incorporated into the 2D parabolic wave equation simulation and tested for frequencies of 75, 150 and 300-Hz; with a point source at a depth of 60m. Both forms were then tested for the more realistic wave packet (three waves) scenario. Both tests showed that the Gaussian soliton is an excellent approximation to the traditional form. Large differences were observed only for initially low energy modes but as the low energy modes contribute virtually nothing to the total acoustic pressure field they can be ignored.

Acoustic propagation through a Gaussian form soliton, and a soliton packet was then simulated. The solitons were moved from 1.5km to 3km range from the sound source, at 5m increments for the single wave case with a 60m source; and at 10m increments for all remaining cases. The mode amplitudes were then plotted for each incremental step. The simulation was run for frequencies of 75, 150 and 300-Hz and for source depths of 60m (submarine case) and 10m (surface ship case) respectively. The following main points were observed: Firstly there was no repeating pattern in mode energies as a function of soliton position; secondly, at higher frequencies the mode energy had larger changes as a function of soliton range; and finally, the pattern of energy change was more structured at higher frequency. The simulation was compared to the theoretical results produced by weak scattering theory to firstly see if the theory was valid, and secondly, to use the theory to explain the results obtained in the simulation.

For all cases excellent agreement was observed between the simulation and the theory. Although a poor comparison for 300-Hz was expected (as the theory is only calculated to the first order) the close comparison in both the mode shapes and energy

values was surprising. Even though the results remained consistently good for all cases (even at 300-Hz), there was a slight tendency for the theory to over predict mode energy values at higher frequencies.

Some low energy modes did contribute to discrepancies between the results. Whilst not all low energy modes added to the discrepancies, it is believed that the theory did not handle mode coupling from high to low energy, or vice versa, as effectively as coupling between two relatively low energy modes; since the theory is a single, weak scattering approach.

For all wave packet cases very little difference was observed in the mode pattern compared to the single wave cases. This leads to the conclusion that, at the frequencies trialed, mode coupling is dominated by the first wave in the packet. Higher frequencies will need to be tested to determine when the pattern is significantly affected by other waves in the packet.

It is expected that the discrepancies observed between the simulation and the theoretical results will be resolved with higher order theory but it is clear that even with only first order results, the acoustic pressure field can be accurately predicted in both a single and a multi-wave, soliton environment. Using this premise, the theory (Equations (36) and (37)) were used to explain the observations made with the simulation.

A plot of horizontal wave number versus mode number was constructed using the theory and showed a non linear relationship between the two terms. This lead to the conclusion that horizontal wave numbers and mode numbers are not commensurate, thus explaining the non-periodic structure of $|A_n|^2(r_0)$. The coupling terms of the modal evolution equation were also plotted and showed that they always act to increase coupling strength with increasing frequency. The reason not all modes increase in coupling strength with frequency was explained by the complex nature of the excitation energy term in Equation (37). This term can either magnify or diminish the increase in coupling strength with frequency, caused by the coupling matrix terms. The increase in structure as a function of range, with increasing frequency, was clearly caused by the increase in allowable difference wave numbers l_{mn} with increasing frequency. This was

governed by the phase term in the modal evolution equation, which is the only one dependent on the soliton position.

It is recommended that future research test higher order theory against simulation to determine if the discrepancies observed in the first order theory can be resolved, particularly for the low energy modes. Both the theory and the model need to include density and bottom attenuation to represent a more realistic study. The theory may also be modified to include stochastic soliton parameters like amplitude, width and wavepacket shape; and to predict other observables like total pressure field scintillation, phase variance, or coherence. Finally, a “real world” study will be required to prove the validity of the weak scattering theory in a soliton environment.

These preliminary results on acoustic field predictability in a simulated single and multi-wave soliton environment are very promising. This research is the first step in moving from a state of observing acoustic propagation through solitons, to one of predicting it. It is expected that with further research, soliton models and weak scattering theory will ultimately be incorporated into sonar prediction software, thus providing more accurate acoustic range predictions in littoral waters.

THIS PAGE INTENTIONALLY LEFT BLANK

LIST OF REFERENCES

- Chiu, C. (1998). Realistic simulation studies of acoustic signal coherence in the presence of an internal soliton wavepacket. Mar 29, 2006, from <http://www.whoi.edu/science/AOPE/ISW98workshop/text/chiu/chiu.htm>.
- Colosi, J.A., & Flatté S. M. (1996). Mode coupling by internal waves for multimegahertz acoustic propagation in the ocean. *Journal of Acoustical Society of America*, 100 (6), 3607-3620.
- Colosi, J.A. (2006). Sound through solitons. (Class notes, Naval Postgraduate School, 2006).
- Duda, T.F., & Preisig, J.C. (1999). A modeling study of acoustic propagation through moving shallow-water solitary wave packets. *IEEE Journal of Oceanic Engineering*, 24 (1), 16-32.
- Jensen, F.B., Kuperman, W.A., Porter, M.B., & Schmidt, H. (2000). *Computational ocean acoustics*. New York: AIP Press.
- Preisig, J.C., & Duda, T.F. (1997). Coupled acoustic mode propagation through continental-shelf internal solitary waves. *IEEE Journal of Oceanic Engineering*, 22 (2), 256-269.
- Shang, E.C., Wang, IA., & Ostrovsky, L. (1998). Acoustical impacts and inversion scheme on internal solitary waves. Mar 29, 2006, from <http://www.whoi.edu/science/AOPE/ISW98workshop/text/shang/shang.htm>.
- U. S. Marine Corps. (1992), *From the Sea* (Navy News Service 048/92), Headquarters, US Marine Corps.
- Warn-Varnas, A.C., Chin-Bing, S.A., King, D.B., Brandt, P., Rubino, A., Martin, P., et al. (1998). Modeling the effects of solitons on acoustics. Mar 29, 2006, from <http://www.whoi.edu/science/AOPE/ISW98workshop/text/varnas/varnas.htm>.
- Weisstein, E.W. (2006a). Soliton. Mar 29, 2006. from <http://mathworld.wolfram.com/Soliton.html>.
- Weisstein, E.W. (2006b). Kortweg-de Vries equation. Mar 29, 2006. from <http://mathworld.wolfram.com/Kortweg-deVriesEquation.html>.
- Zhou, J., Zhang, X., & Rogers, P. (1991). Resonant interaction of sound wave with internal solitons in coastal zone. *Journal of Acoustical Society of America*, 90 (4), 2042-2054.

THIS PAGE INTENTIONALLY LEFT BLANK

INITIAL DISTRIBUTION LIST

1. Defense Technical Information Center
Ft. Belvoir, Virginia
2. Dudley Knox Library
Naval Postgraduate School
Monterey, California
3. Professor John Colosi, Department of Oceanography
Naval Postgraduate School
Monterey, California
4. Professor D. Benjamin Reeder
Naval Postgraduate School
Monterey, California
5. Professor Mary Batteen, Chair
6. CMDR Andrew McCrindell
Directorate of Oceanography and Meteorology
Sydney, NSW, Australia
7. LCDR Aaron Young
Directorate of Oceanography and Meteorology
Sydney, NSW, Australia